Surface deformations caused by pressurized finite ellipsoidal cavities

Mehdi Nikkhoo[1,1] and Eleonora Rivalta[1,1]

[1]GFZ German Research Centre for Geosciences

November 30, 2022

Abstract

Volcano deformation monitoring is fundamental to detect pressurizations of magma bodies and forecasting any ensuing eruptions. Analytical and quasi-analytical solutions for pressurized cavities are routinely used to constrain volcano deformation sources through inversion of surface displacement data. Due to their computational efficiency, such solutions enable a thorough exploration of the parameter space and thereby provide insight into the physics of magma-rock interaction. Developing more general deformation models can help us better characterize subsurface magma storage. We develop quasi-analytical solutions for the surface deformation field due to the pressurization of a finite (triaxial) ellipsoidal cavity in a half-space. The solution is in the form of a non-uniform distribution of triaxial point sources within the cavity. The point sources have the same aspect ratio, determined by the cavity shape, while their strengths and spacing are determined in an adaptive manner, such that the net point-source potency per unit volume is uniform. We validate and compare our solution with analytical and numerical solutions. We provide computationally-efficient MATLAB codes tailored for source inversions. This solution opens the possibility of exploring the geometry of shallow magma chambers for potential deviations from axial symmetry.

Surface deformations caused by pressurized finite ellipsoidal cavities

Mehdi Nikkhoo[1,2] and Eleonora Rivalta[1,3]

[1] *GFZ German Research Centre for Geosciences, Potsdam, Germany. E-mail: mehdi.nikkhoo@gfz-potsdam.de*

[2] *The Abdus Salam International Center for Theoretical Physics, Trieste, Italy,*

[3] *Department of Physics and Astronomy, Alma Mater Studiorum University of Bologna, Italy.*

SUMMARY

Volcano deformation monitoring is fundamental to detect pressurizations of magma bodies and forecasting any ensuing eruptions. Analytical and quasi-analytical solutions for pressurized cavities are routinely used to constrain volcano deformation sources through inversion of surface displacement data. Due to their computational efficiency, such solutions enable a thorough exploration of the parameter space and thereby provide insight into the physics of magma-rock interaction. Developing more general deformation models can help us better characterize subsurface magma storage.

We develop quasi-analytical solutions for the surface deformation field due to the pressurization of a finite (triaxial) ellipsoidal cavity in a half-space. The solution is in the form of a non-uniform distribution of triaxial point sources within the cavity. The point sources have the same aspect ratio, determined by the cavity shape, while their strengths and spacing are determined in an adaptive manner, such that the net point-source potency per unit volume is uniform. We validate and compare our solution with analytical and numerical solutions. We provide computationally-efficient MATLAB codes tailored for source inversions. This solution opens the possibility of exploring the geometry of shallow magma chambers for potential deviations from axial symmetry.

Key words: Geomechanics; Kinematics of crustal and mantle deformation; Physics of magma and magma bodies; Volcano monitoring.

1 INTRODUCTION

Volcano deformation is an indicator of ongoing fluid transport or pressure build-up within magma reservoirs and is often a reliable precursor to eruptions (Dvorak & Dzurisin 1997; Dzurisin 2006). Pressurization of magma chambers may be caused by replenishment with new magma from below, or degassing of the magma residing in the chamber (Edmonds & Woods 2018; Degruyter et al. 2019; Trasatti et al. 2019; Hill et al. 2020; Wicks et al. 2020; Caricchi et al. 2021). Pressure may also build up within shallow magma bodies, such as lava domes (Salzer et al. 2014; Wang & Aoki 2019), or hydrothermal reservoirs due to rapid ascent of volatiles or magma-water interaction (Kobayashi et al. 2018; Ueda et al. 2018; Narita et al. 2020; Yunjun et al. 2021). Magma bodies may also expand, or contract, due to thermal effects (Furuya 2004, 2005; Wang & Aoki 2019). Critically pressurized magma chambers may rupture leading to injection of a magmatic dike and ensuing chamber depressurization (Narita et al. 2019). These processes may generate measurable surface deformations (Dvorak & Dzurisin 1997; Dzurisin 2000; Lu & Dzurisin 2014; Biggs & Pritchard 2017), which can be evaluated through mathematical models to infer the source parameters: the shape, location, spatial orientation and volume change (Dvorak & Dzurisin 1997; Dzurisin 2003; Lisowski 2007; Segall 2010). Such analyses have immensely contributed to our understanding of volcanic processes (Dvorak & Dzurisin 1997; Dzurisin 2006; Segall 2010). This has motivated both advancing the technologies for acquiring deformation data with higher spatio-temporal resolutions (Pinel et al. 2014; Poland & Zebker 2022), and developing new analytical and numerical deformation source models (Amoruso & Crescentini 2011; Segall 2016; Nikkhoo et al. 2017).

Analytical or quasi-analytical source models, which are fast to compute and need no expert setup, are key assets for these inversions during volcanic crises (Beauducel et al. 2020a,b) or for in-depth studies of multiple eruptive cycles over extended time periods (Amoruso et al. 2014; Lisowski et al. 2021; Bruno et al. 2022). This has motivated the development of several new analytical source inversion software packages (Battaglia et al. 2013; Bagnardi & Hooper 2018; Cannavó 2019; Beauducel et al. 2020a; Heimann et al. 2019; Vasyura-Bathke et al. 2019, 2020; Trasatti 2022). Moreover, analytical solutions can be used as components of both data assimilation frameworks (Bato et al. 2017; Zhan et al. 2017) and physical volcano deformation models describing the evolution of the plumbing systems (Anderson & Segall 2011, 2013; Anderson & Poland 2016). New generalized analytical solutions would offer more flexibility for all these applications.

The surface displacements caused by deep volumetric deformation sources can be adequately modelled through point-source models such as the point spherical (Mogi 1958), point spheroidal (Davis et al. 1974) and point ellipsoidal (Davis 1986) models. A triaxial point-source model that includes the mentioned solutions as special cases is the point Compound Dislocation Model (point CDM; Nikkhoo et al. 2017).

McTigue (1987) and Yang et al. (1988) showed that point sources (Mogi (1958) and Davis (1986) models, respectively) fail to properly simulate the near-field surface displacements associated with shallow pressurized cavities if the depth to semi-major axis ratio of the cavity is smaller than 2. In the case of pressurized penny-shaped cracks, a point tensile dislocation can adequately simulate the near-field surface displacements if the depth to semi-major axis ratio is greater than 5 (Sun 1969; Fialko et al. 2001). This is because the near-field displacements are affected by the finite dimension of the source. For such cases, finite source models are required to constrain all source parameters reliably (Lisowski 2007; Segall 2010). The most commonly-used finite source models of uniform pressure are the finite spherical (McTigue 1987), finite spheroidal (Yang et al. 1988) and penny-shaped crack (Sun 1969; Fialko et al. 2001) models. As these models are all axisymmetric, they cannot properly represent the deformation field caused by triaxial sources.

After Eshelby (1957), a solution for a uniformly pressurized finite ellipsoidal cavity in the full space can be obtained by appropriate triaxial point sources uniformly distributed throughout the cavity (Yang et al. 1988; Segall 2010). Davis et al. (1974) and Davis (1986) incorporated the Mindlin (1936) half-space Green's functions instead of the full-space Green's functions into the Eshelby's solution, a procedure that we call below the "Davis approximation", to derive their approximate half-space point-source solution. Similarly, Yang et al. (1988) used the Davis approximation to develop a closed-form, approximate solution for finite prolate spheroids. Cervelli (2013) extended the Yang et al. (1988) solution to a model for both prolate and oblate spheroids. Yang et al. (1988) also showed for vertical prolate spheroids that, as a rule of thumb, the solution is fairly accurate if the depth to the top of the spheroid is larger than the radius of curvature at the spheroid top.

Amoruso & Crescentini (2011) proposed a multipole expansion up to quadrupole terms of the Eshelby (1957) solution as a finite-source model for pressurized triaxial ellipsoids—the closed-form analytical expression of this model were provided later by Amoruso & Crescentini (2013). Moreover, Amoruso & Crescentini (2011) developed a configuration composed of 7 triaxial point sources (Davis 1986) of appropriate strength and location (one source at the center and six sources located symmetrically on the axes of the ellipsoidal cavity). They showed that the 7-point source solution is in good agreement with the closed-form analytical version of their model. Amoruso & Crescentini (2011) also compared the 7-point-source model with the Davis (1986), McTigue (1987), Yang et al. (1988) and

Fialko et al. (2001) models. However, the comparisons did not explore a wide range of source parameters, especially for shallow sources. To our knowledge, the Amoruso & Crescentini (2013) analytical solution has been compared only with the 7-point-source solution, and only for 3 cavities with d_C/a_C of 1.88 and 3.75 (see supporting information in Amoruso & Crescentini 2011). Thus, the range of applicability of the Amoruso & Crescentini (2011) and Amoruso & Crescentini (2013) models is not clear. At present, solutions properly-validated for shallow ellipsoidal sources along with computer programs suitable for inversions are yet to be developed and adopted by the community.

In principle, it is straightforward to follow Eshelby (1957) and use the Davis approximation to derive a half-space solution for finite ellipsoids in the form of an evenly-spaced distribution of triaxial point sources. Amoruso et al. (2007) applied this approach to simulate the surface displacements of a finite horizontal penny-shaped crack, showing that the solution is accurate if the depth-to-radius ratio is larger than 0.8. However, there are at least two issues with this approach when generic finite triaxial sources are considered. First, the spacing between the point sources needs to be chosen carefully such that accurate results are achieved within reasonable computation times, which are imposed by the application type. Specifically, rapid inversions require a large number of forward calculations to be performed within a few hours or in a day—this narrows down the acceptable computation time for a single forward simulation to a few seconds. The second issue is that the optimal point-source spacing should be defined in a fully automatic way for any cavity geometry and accuracy requirement. This is because it is plausible that the optimal spacing depends on the aspect ratio, orientation and depth of the cavity. Adopting the same small spacing for all cavity geometries, or requiring the user to adapt spacing to each geometry explored during the inversion, would be inefficient or even impractical.

Here we propose that a solution for the surface displacements associated with finite cavities can be developed in the form of a non-uniform distribution of point sources (here point CDMs) with depth-dependent spacing and strengths. This way, fewer, but larger magnitude, point sources are distributed at deeper locations within the cavity. We first introduce an adaptive algorithm that involves a set of analytical solutions controlling the location, spacing and strengths of the point CDMs. Next, we compare our solutions with published results from analytical and numerical models. Finally, we discuss the advantages, limitations and the implications of the new solution for inversions involving deformation data as well as joint inversions of deformations and gravity changes.

2 METHODS

2.1 A new adaptive configuration

In the following we develop a solution for uniformly pressurized ellipsoidal cavities in a homogeneous, linear, elastic half-space with Poisson's ratio, ν, and bulk modulus, K. We refer to this solution as the finite Ellipsoidal Cavity Model (finite ECM). We adopt a Cartesian right-handed xyz coordinate system with the origin on the free surface and the z axis pointing upward. The parameters defining a finite ECM are: the coordinates of its center $(x_0, y_0, -d_\mathrm{C})$, where d_C is the depth to the center of the cavity, the semiaxes (a_x, a_y, a_z), the rotation angles $(\omega_x, \omega_y, \omega_z)$ and the overpressure δp. If the rotation angles are zero, a_x, a_y and a_z are aligned with the x, y and z axes, respectively.

To implement the solution based on the the Eshelby (1957) and the Davis approximation, we distribute within the cavity a set of expanding triaxial point sources. Such triaxial point sources can be formed as a superposition of three mutually orthogonal force dipoles (Mindlin 1936; Davis 1986), or alternatively, three mutually orthogonal point tensile dislocations (Lisowski et al. 2008; Bonafede & Ferrari 2009). Here we employ the point CDM (Nikkhoo et al. 2017), which implements the latter configuration. The potencies of the three individual point dislocations (the product of opening and surface area) define the aspect ratio and the strength of the point CDM.

The far-field deformations due to any ellipsoidal cavity can be represented by a point CDM located at the cavity center and having potencies

$$\begin{pmatrix} \Delta V_x \\ \Delta V_y \\ \Delta V_z \end{pmatrix} = \frac{-V \delta p}{3K} (\mathbf{S} - \mathbf{I}_3)^{-1} \begin{pmatrix} 1 \\ 1 \\ 1 \end{pmatrix}, \tag{1}$$

where $V = \frac{4\pi}{3} a_x a_y a_z$ is the volume of the cavity, $\mathbf{I_3}$ is the identity matrix and

$$\mathbf{S} = \begin{pmatrix} S_{1111} & S_{1122} & S_{1133} \\ S_{2211} & S_{2222} & S_{2233} \\ S_{3311} & S_{3322} & S_{3333} \end{pmatrix},$$

where S_{iijj} are the Eshelby (1957) tensor components, with the indices 1, 2 and 3 indicating the x, y and z directions, respectively (Nikkhoo et al. 2017). The terms S_{iijj} are nonlinear functions of a_x, a_y, a_z and ν (see Eshelby 1957; Amoruso & Crescentini 2009; Segall 2010). Let a_C denote the characteristic dimension (semi-major axis) of the cavity:

$$a_\mathrm{C} = \max\{a_x, a_y, a_z\}. \tag{2}$$

The point-source approximation is accurate if the distance between the cavity and the observation points—here d_C—is much larger than a_C (Sun 1969; McTigue 1987; Fialko et al. 2001; Segall 2010).
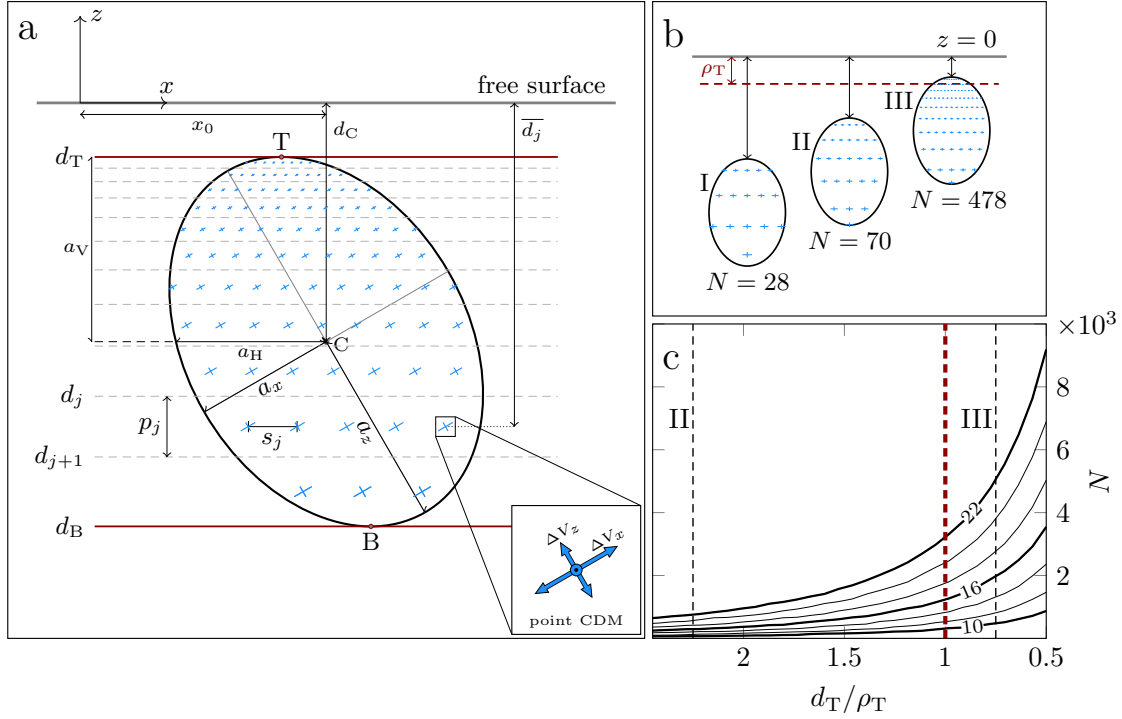
Figure 1. a) The adaptive source model for $c_r^* = 10$. The ellipsoid parameters are: center at $(x_0, 0, -d_C)$, $a_x/a_z = 0.714$, $a_z/d_C = 0.826$, $\omega_x = \omega_z = 0°$ and $\omega_y = 30°$. d_T and d_B are the depths to the ellipsoid top (T) and bottom (B), respectively. $d_T/d_C = 0.226$ and $d_B/d_C = 1.774$. Red lines: uppermost and lowermost partitioning planes. The j-th partition is bounded by the ellipsoid and partitioning planes (dashed lines) at depths d_j and d_{j+1}. Cross symbols are the point CDMs, with a total number $N = 879$. Inset: point CDM configuration. For this ellipsoid geometry and for $\nu = 0.25$, $\Delta V_z/\Delta V_x = 0.671$. b) Adaptive source model ($c_r^* = 10$) for the same ellipsoid as in a) but with $\omega_x = \omega_y = \omega_z = 0°$. a_z/d_C is 0.344, 0.466 and 0.724 for I, II and III, respectively. d_T/ρ_T is 3.75, 2.25 and 0.85 for I, II and III, respectively. c) For the same source geometry as in panel b), the solid curves show N, for c_r^* varying between 10 and 22, as a function of d_T/ρ_T. Numbers on the thick curves indicate c_r^*. The vertical dashed line is $d_T = \rho_T$, which represents the Yang et al. (1988) rule of thumb. Note that for the tilted cavity in a) $\rho_T/a_z = 0.620$, whereas for the cavities in b) we have $\rho_T/a_z = 0.510$.

The approximation error is, thus, a function of the ratio

$$c_r = \frac{d_C}{a_C}. \tag{3}$$

Following Eshelby (1957), the near-field deformations of a finite ellipsoidal cavity can be represented by a set of point CDMs—with potencies proportional to those in equation 1—continuously distributed throughout the cavity. Each point CDM of the set can be interpreted as an "auxiliary ellipsoid", that is, an infinitesimal ellipsoidal cavity with the same aspect ratio, pressure and spatial orientation as the finite cavity. In practice, a finite number of point CDMs can approximate the near-field solution with arbitrary accuracy. By trial and error we found that satisfactory results are achieved

if: 1) the point CDM spacing is such that the auxiliary ellipsoids are regularly packed (ellipsoids tangent to each other at the tips of their axes), and 2) the c_rs associated with the auxiliary ellipsoids are larger than a certain threshold, c_r^*, which we refer to as the "grid-spacing parameter" (section 2.3). Thus, if the semi-axes of the auxiliary ellipsoids are $a'_x = ka_x$, $a'_y = ka_y$, $a'_z = ka_z$, where $k < 1$ is a scale factor, the spacing between the point CDMs in the three directions becomes $2ka_x$, $2ka_y$, $2ka_z$, respectively. Denoting the depth to the top and bottom of the ellipsoidal cavity with d_T and d_B, respectively, and defining

$$a_V = (d_B - d_T)/2, \tag{4}$$

as half of the vertical extent of the cavity (see Fig. 1a), the c_r for the shallowest auxiliary ellipsoid will be

$$c'_r = \frac{d'_C}{a'_C} = \frac{d_T + ka_V}{ka_C}, \tag{5}$$

where d'_C and a'_C are the depth to the center and semi-major axis of the shallowest auxiliary ellipsoid, respectively. We note that $2a_V$ is the vertical extent of the cavity and $2ka_V$ is the vertical extent of the auxiliary ellipsoids. For a given c_r^*, equation 5 can be solved for k, which determines the point CDM spacing. The potencies of the point CDMs in this configuration are $(\Delta V_x/N, \Delta V_y/N, \Delta V_z/N)$, where ΔV_x, ΔV_y and ΔV_z are calculated from equation 1 and N is the total number of the point CDMs. Numerical convergence tests show that $c_r^* = \sim 10$ provides very good results (see section 2.3), but it may lead to a large N and thus, long computation times.

To address this problem, we have devised a new configuration in which the size of the auxiliary ellipsoids increases with depth such that they all have the same c_r. In this new configuration the auxiliary ellipsoids are regularly packed in horizontal layers stacked on top of each other. The vertical extent of the layers—that is, the vertical extent of the auxiliary ellipsoids—are obtained from top to bottom through an iterative procedure. Assuming $c'_r = c_r^*$, from equation 5 we calculate the scale factor for the auxiliary ellipsoids on the top layer as

$$k_1 = d_T/(c_r^* a_C - a_V), \tag{6}$$

from which the vertical extent of the first layer can be calculated as $2k_1 a_V$. The depth to the top of the second layer is then

$$d_2 = d_T(1 + 1/n_p), \tag{7}$$

where

$$n_p = d_T/(2k_1 a_V). \tag{8}$$

Using d_2 in place of d_T, and the same c_r^*, in equation 5, we determine k_2 and thus, the vertical extent of the second layer. By repeating this procedure, we determine the depths, and thus the vertical extents,

of further layers. Now we determine the point CDM spacing and potencies in each layer. Let a_H and a_h denote the semi-major axis and semi-minor axis, respectively, of the horizontal ellipse formed by the intersection of the ellipsoidal cavity and a horizontal plane passing through its center. The spacing of the point CDMs in the j-th layer will be $2k_j a_\mathrm{H}$ and $2k_j a_\mathrm{h}$ in the directions parallel to a_H and a_h, respectively. Finally, we adjust the point CDM potencies in each layer such that the potency per unit volume remains uniform throughout the cavity.

The new configuration is obtained through the following adaptive algorithm:

1. We set c_r^* depending on the desired accuracy or the maximum total number of allowed point CDMs, N_max.

2. We determine d_T and d_B analytically (Appendix A) and then calculate n_p from equation 8.

3. We partition the cavity by using the planes $z = -d_\mathrm{T}$, $z = -d_\mathrm{B}$ and $z = -d_j$, where $d_j = d_\mathrm{T}\left(1 + 1/n_\mathrm{p}\right)^{j-1}$, $j = 2, 3, \ldots, M - 1$ (dashed lines in Fig. 1a) in which M is the number of partitioning planes.

4. We calculate the volumes V_j of the cavity partitions analytically (see Appendix B).

5. We determine analytically the ellipses formed by the intersections of the cavity and the planes $z = -\overline{d_j} = -(d_j + d_{j+1})/2$ passing through the middle of the partitions (see Fig. 1a and Appendix C).

6. On every intersection ellipse we create a regular grid of point CDMs such that one point CDM lies at the center of the ellipse (Fig. 1a). As the grid spacing parallel to a_H and a_h we use $s_j^\mathrm{H} = 2k_j a_\mathrm{H}$ and $s_j^\mathrm{h} = 2k_j a_\mathrm{h}$, respectively, where $k_j = d_j/(c_\mathrm{r}^* a_\mathrm{C} - a_\mathrm{V})$. N_j and N denote the total number of point CDMs within the j-th partition and within the cavity, respectively. Note that every partition will contain at least one point CDM at its center.

7. For the top and bottom partitions, we calculate h_i', for $i = 1, \ldots, N_j$, as the vertical distance between each point CDM and the cavity surface.

8. We set the potencies of the point CDMs as $(\alpha_{ij}\frac{V_j}{V}\Delta V_x, \alpha_{ij}\frac{V_j}{V}\Delta V_y, \alpha_{ij}\frac{V_j}{V}\Delta V_z)$, where for the top and bottom partitions ($j = 1$ and $j = M - 1$) $\alpha_{ij} = h_i/\sum_{k=1}^{N_j} h_k$ in which $h_i = h_i' + k_j a_\mathrm{V}$, and for all the other partitions $\alpha_{ij} = 1/N_j$.

9. We calculate the volume change, δV, associated with the finite ECM from the Eshelby (1957) solution. The calculated volume change corresponds to a pressurized cavity in full space (see section 4.3).

10. We calculate $d_\mathrm{T}/\rho_\mathrm{T}^\mathrm{max}$ and $d_\mathrm{T}/\rho_\mathrm{T}^\mathrm{min}$, where $\rho_\mathrm{T}^\mathrm{max}$ and $\rho_\mathrm{T}^\mathrm{min}$ are the maximum and minimum radii of curvature at T, respectively (Appendix D). Later, we consider $d_\mathrm{T}/\rho_\mathrm{T}^\mathrm{max}$ and $d_\mathrm{C}/a_\mathrm{C}$ of the cavity for further assessment of the solution quality.

2.2   Computational efficiency of the finite ECM

The computation time associated with the finite ECM depends on N. For a specific c_r^* in the adaptive algorithm, N is determined by the shape (aspect ratio and size), depth and spatial orientation of the cavity (Fig. 1a-c). The non-linear link between the cavity depth and N can be better appreciated in Fig. 1b-c, where a varying depth for cavities of the same shape and orientation leads to different values for N. As the source gets very shallow, N becomes very large. However, we have to keep in mind that, similar to the Yang et al. (1988) solution, the accuracy of the finite ECM degrades if the source is too shallow. Thus, by applying some source-quality criteria, very large values for N can be automatically excluded. According to Yang et al. (1988), $d_T \gtrsim \rho_T$ defines, as a rule of thumb, a minimum depth for vertical prolate cavities (cavity top below the dashed line in Fig 1b). For such cavities, N does not exceed a few thousands, even for $c_r^* = 22$ (left-hand side of the red dashed line in Fig 1c), which is much larger than needed for an excellent solution (Section 2.3).

Once c_r^* is fixed in the adaptive algorithm, the shallower the cavity, the higher the computational efficiency achieved by using the adaptive configuration in comparison with an evenly-spaced configuration. For example for the cavity in Fig 1a, the N for the evenly-spaced configuration of equivalent accuracy is 21.5 times larger than the N for the adaptive configuration. Similar factors calculated for the first (I), second (II) and third (III) cavities in Fig 1b are 1, 2.7, 14.4, respectively. For a given c_r^*, N also depends on the other source parameters beside the cavity depth.

The finite ECM involves computing the surface displacements for N point CDMs on the same grid of observation points. Thus, similar to Beauducel et al. (2020b), we achieved further computational efficiency through a full vectorization of the original point CDM computer codes. From experimenting with the codes, we verified that the computation time associated with the finite ECM scales roughly linearly with the number of point CDMs. As an example, the computation of surface displacements at 100 observation points caused by a configuration of $N = 1000$ point CDMs requires 0.12 seconds on a personal computer (with 2.80 GHz processor with 8 threads). Similar computations for $N = 10000$ and $N = 20000$ point CDMs require 1.3 and 2.4 seconds, respectively. The adaptive algorithm along with the vectorization speed up the computation times sufficiently to render the finite ECM suitable for rapid source inversions, akin to conventional analytical solutions.

2.3   Calibration of the grid-spacing parameter

As stated earlier, the accuracy of the solution depends on c_r^*. In order to calibrate c_r^*, we use the only exact solution for finite non-spherical sources, namely, the Yang et al. (1988) solution for spheroidal cavities. We conduct systematic comparisons between the finite ECM and the Yang et al. (1988) surface displacements for ~ 7500 oblate and prolate spheroids with various aspect ratios, depths and

dip angles (see caption of Table 1). To do so, we calculate the surface displacements associated with the Yang et al. (1988) solution on a regular grid of points using the MATLAB codes provided by Cervelli (2013) and Battaglia et al. (2013). Next, on the same grid, we calculate the surface displacements using the finite ECM for various c_r^*. As measures of the deviation between the two solutions we calculate $\epsilon_x = \max\{(u_x^{(1)} - u_x^{(2)})/u_z^{(2)}\}$ and $\epsilon_z = \max\{(u_z^{(1)} - u_z^{(2)})/u_z^{(2)}\}$, where the "max" is calculated over all observation points, superscript "(1)" refers to the finite ECM and superscript "(2)" refers to the Yang et al. (1988) solution. We evaluate both the maximum of these deviations among all models, and the fraction of models where ϵ_x and ϵ_z are below 0.01. In order to avoid errors due to normalizing by near-zero vertical displacements, we limit the calculation to observation points with a vertical displacement larger than 10 per cent of the maximum vertical displacement on the grid. Results confirm that already with $c_r^* = 10$ a very good accuracy is obtained. An excellent accuracy, sufficient for most practical applications, is reached with $c_r^* = 12$ for prolate sources and $c_r^* = 14$ for oblate sources. A similar analysis for triaxial ellipsoids is only possible through a convergence test. Using solutions with $c_r^* = 20$ as the benchmark, we find that setting $c_r^* = 12$ leads to an excellent accuracy for triaxial ellipsoids (see Table 1).

3   COMPARISON TO PUBLISHED ANALYTICAL AND NUMERICAL SOLUTIONS

We compare the finite ECM with published analytical and numerical solutions. We choose source parameters close to the limits of the range of applicability of the finite ECM. Unless otherwise stated, we use $c_r^* = 14$ and $N_{\max} = 4000$. Note that when comparing two solutions, displacements are commonly normalized in two different ways: method I) Both solutions normalized by the maximum vertical displacement of one of the solutions; method II) Each solution normalized by its own maximum vertical displacement. First, we compare the finite ECM with analytical solutions and next with numerical solutions for triaxial ellipsoids. We use normalization method I in our analytical comparisons (Fig. 2) and both normalization methods I and II in the numerical comparisons (Fig. 3). We later expand on the implications of the normalization methods.

For the first analytical comparison we consider the Yang et al. (1988), Amoruso & Crescentini (2011) and Amoruso & Crescentini (2013) solutions (Fig. 2a). The source in this case is a prolate spheroid with $a_x/a_z = 1/3$ and $a_z/d_C = 5/6$. Despite the rather low $d_C/a_C = 1.2$ of the cavity, the displacements from the finite ECM and Yang et al. (1988) solution are in excellent agreement. In contrast, the Amoruso & Crescentini (2011) and Amoruso & Crescentini (2013) models underestimate the near-field surface displacements by almost 20%. Comparisons similar to that illustrated in Fig. 2a show that the Amoruso & Crescentini (2011) and Amoruso & Crescentini (2013) models perform well for a range of rather shallow, vertically-elongated sources.
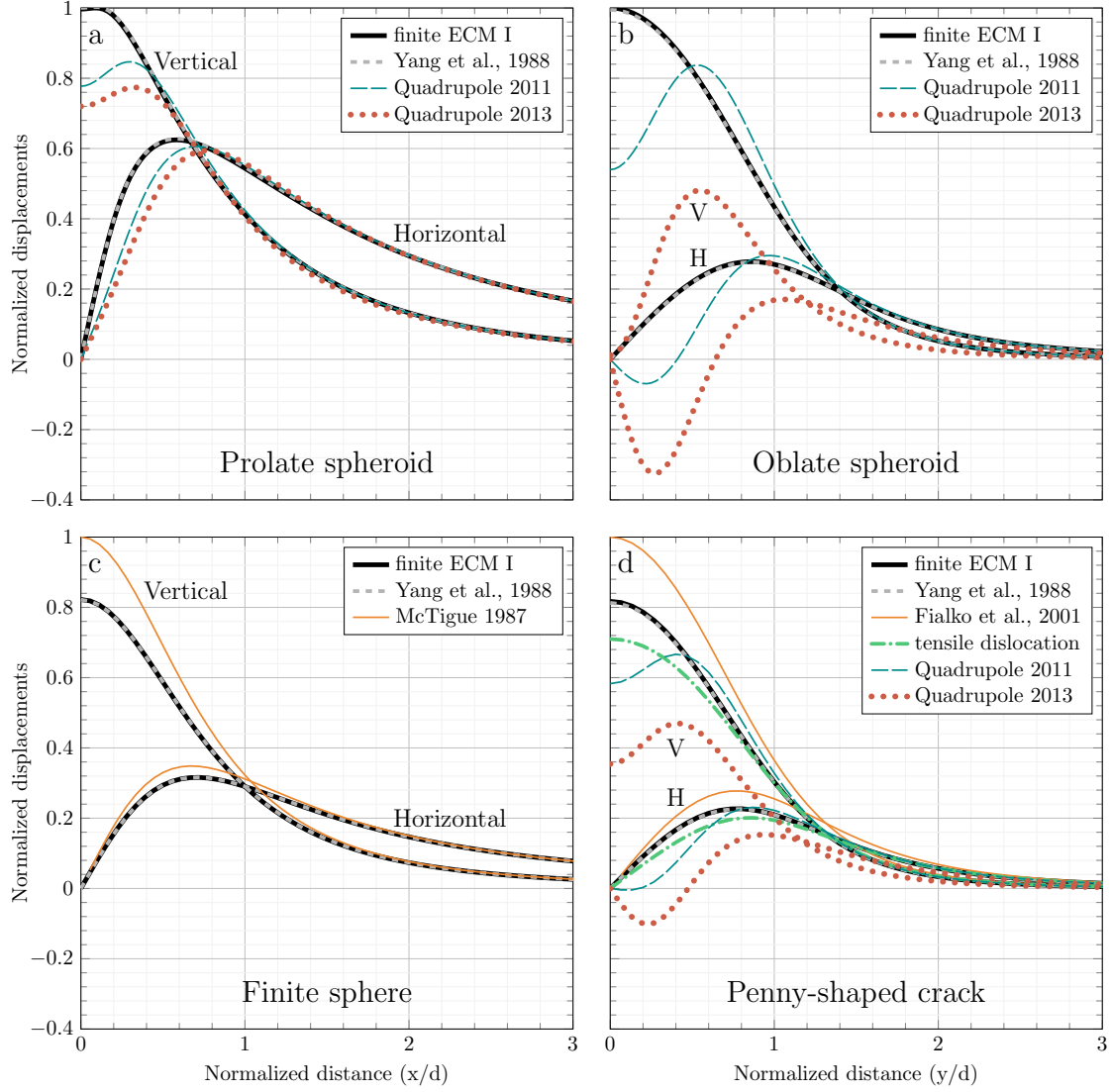
Figure 2. Comparison of the finite ECM with selected analytical solutions. "Quadrupole 2011" and "Quadrupole 2013" refer to the Amoruso & Crescentini (2011) and Amoruso & Crescentini (2013) models. For all displacements, normalization method I has been used. The horizontal and vertical displacements are indicated in a) and c). The curves below "H" and those above "V" in b) and d) represent the horizontal and vertical displacements, respectively. In all cases $\omega_x = \omega_y = \omega_z = 0°$. a) Comparison with a prolate spheroid. Source parameters are $a_x/a_z = 1/3$, $a_x = a_y$ and $a_z/d_C = 5/6$, and $N = 3297$. b) Comparison with an oblate spheroid. Source parameters are $a_x/a_z = 18$, $a_x = a_y$ and $a_z/d_C = 1/18$, and $N = 1439$. c) Comparison with the finite spherical source. Source parameters are $a_x = a_y = a_z = R$ and $R/d_C = 0.556$, and $N = 385$. d) Comparison with the penny-shaped crack and a square tensile dislocation (Okada 1985). Source parameters are $a_z/a_x = 10^{-6}$, $a_x = a_y$ and $a_x/d_C = 0.867$, and $N = 933$. The square dislocation has the same potency as the finite ECM and its edge length is $(\pi a_x^2)^{1/2}$.

Table 1. Systematic comparison of the Yang et al. (1988) solution (prolate and oblate spheroids) with the finite ECM for varying c_r^*, and convergence test of the finite ECM for triaxial ellipsoids. $\overline{t_C}$ is the mean computation time, $\max \epsilon_x$ and $\max \epsilon_z$ are the maximum relative errors for the u_x and u_z components of the surface displacements, respectively, and $\alpha(\epsilon_x < 0.01)$ and $\alpha(\epsilon_z < 0.01)$ are the percentages of cases with relative errors below 1 per cent. The comparison involves 3800 prolate spheroids with parameters $x_0 = y_0 = 0\,\text{m}$, $d_C \in [100, 1000]\,\text{m}$, $a_z = 1000\,\text{m}$, $a_x = a_y \in [50, 950]\,\text{m}$, $\omega_x = \omega_z = 0°$, $\omega_y \in [0°, 90°]$. For $c_r^* = 10$, we have $N_{\min} = 20$, $N_{\max} = 2884$, whereas for $c_r^* = 20$ we have $N_{\min} = 163$ and $N_{\max} = 15035$. The comparison also involves 3716 oblate spheroids, with parameters $a_x = a_y = 1000\,\text{m}$ and $a_z \in [50, 950]\,\text{m}$; all the other parameters are the same as those for the prolate sources. For oblate cavities, $c_r^* = 10$ leads to $N_{\min} = 20$ and $N_{\max} = 1413$, and $c_r^* = 20$ results in $N_{\min} = 163$ and $N_{\max} = 11410$. The convergence test involves 5868 triaxial ellipsoids, with parameters $x_0 = y_0 = 0\,\text{m}$, $d_C \in [1000, 2000]\,\text{m}$, $a_x = 1000\,\text{m}$, $a_y \in [50, 950]\,\text{m}$, $a_z \in [50, 950]\,\text{m}$ and $\omega_y \in [0°, 90°]$. For these ellipsoids the finite ECM solution with $c_r^* = 12$ is compared to the solution with $c_r^* = 20$. In all cases, the surface observation grid consists of 496 points with a spacing of $200\,\text{m}$ within $x \in [-3000, 3000]\,\text{m}$ and $y \in [0, 3000]\,\text{m}$. For all sources $d_T \geq 200\,\text{m}$.

c_r^*	$\overline{t_C}$	$\max \epsilon_x$	$\max \epsilon_z$	$\alpha(\epsilon_x < 0.01)$	$\alpha(\epsilon_z < 0.01)$
	[s]	[%]	[%]	[%]	[%]
			Prolate spheroids		
10	0.097	1.2	2.1	98.9	90.0
12	0.17	0.88	1.4	100	98.5
14	0.27	0.76	1.3	100	99.4
20	0.79	0.45	0.73	100	100
			Oblate spheroids		
10	0.10	3.4	4.9	85.0	53.0
12	0.17	2.7	3.5	87.7	80.0
14	0.27	2.1	2.8	99.5	91.3
20	0.80	0.9	1.3	100	99.8
			Ellipsoids		
12	0.40	1.5	2.8	99.7	95.7

The second comparison (Fig. 2b) involves the same analytical solutions, but for an oblate spheroid (Yang et al. 1988; Cervelli 2013) with $a_x/a_z = 18$ and $a_x/d_C = 1$. Again, the finite ECM and the Yang et al. (1988) solutions are almost identical; however, the Amoruso & Crescentini (2011) and Amoruso & Crescentini (2013) models break down with large errors, especially for the horizontal displacements. Interestingly, the Amoruso & Crescentini (2011) solution, which is a finite difference approximation of
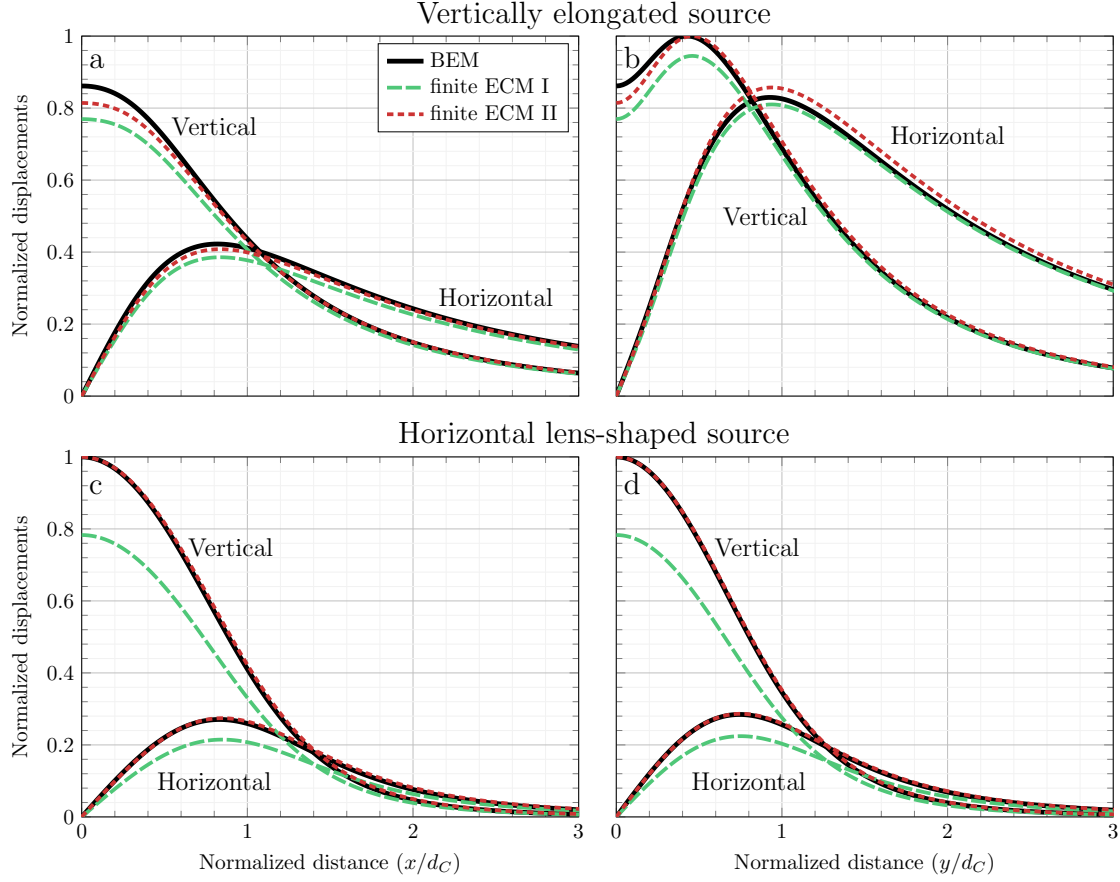
Figure 3. Comparison with selected numerical solutions for triaxial sources. The black solid lines are BEM solutions. The gray and green solid lines are the finite ECM displacements, normalized through methods I and II, respectively (see text). a) Vertically elongated source with $a_x/a_z = 1/2$, $a_y/a_z = 1/3$, $a_z/d_C = 1/2$ and $\omega_x = \omega_y = \omega_z = 0°$. Displacements are shown for the xz plane. b) Same as a), but for the yz plane. c) Lens-shaped source with $a_x/a_z = 15$, $a_y/a_z = 12$, $a_z/d_C = 15$ and $\omega_x = \omega_y = \omega_z = 0°$. Displacements are shown for the xz plane. d) Same as c), but for the yz plane. The finite ECM is shown for $c_r^* = 14$ which leads to $N = 260$ and $N = 1439$ for the vertically elongated source (a and b) and the horizontal lens-shaped source (c and d), respectively.

288   the Amoruso & Crescentini (2013) quadrupole solution, works better than the Amoruso & Crescentini

289   (2013) model. We will expand on the underlying reason later.

290   The next comparison involves the McTigue (1987) and Yang et al. (1988) solutions in the case

291   of a sphere (Fig. 2c). The mismatch between the McTigue (1987) and the Yang et al. (1988) and

292   finite ECM solutions is because both the latter solutions involve the Davis approximation, while the

293   McTigue (1987) solution contains higher-order terms correcting for the resulting misrepresentation

294   of the boundary conditions on the cavity walls. For spherical cavities (except for the McTigue 1987,

295   solution) the surface displacements from the finite-source solutions (Yang et al. 1988, and the finite

ECM) are in theory expected to be identical to their equivalent point-source solutions (Mogi 1958; Davis 1986, and the point CDM). The Amoruso & Crescentini (2011) and Amoruso & Crescentini (2013) models are also comparable to those models. Thus, for the sake of clarity, we only show the McTigue (1987), Yang et al. (1988) and the finite ECM displacements in Fig. 2c.

As the last analytical comparison, we consider a uniformly pressurized penny-shaped crack (Sun 1969; Fialko et al. 2001), the Yang et al. (1988) solution, a horizontal tensile square dislocation (Davis 1983; Okada 1985), and again, the Amoruso & Crescentini (2011) and Amoruso & Crescentini (2013) models. For this special case, the finite ECM has only one layer of point sources with varying potencies. Again, there is an excellent agreement between the finite ECM and the Yang et al. (1988) solution; also the Sun (1969) solution (not shown in Fig. 2d) perfectly agrees with these solutions. The difference with the Fialko et al. (2001) solution is due to the fact that the boundary conditions on the source walls are more accurately implemented in the Fialko et al. (2001) solution. However, compared to the square dislocation, the finite ECM and the Yang et al. (1988) solutions provide a better approximation to the Fialko et al. (2001) solution. This is because the opening of the square dislocation is uniform while the opening of the cracks represented by the Yang et al. (1988) solution and finite ECM have an elliptic form. This feature is implemented through step "7" of the adaptive algorithm. Also in this case, the Amoruso & Crescentini (2011) solution performs better than the Amoruso & Crescentini (2013) model. Both models, however, perform well only in the far field.

Finally, we compare the finite ECM with numerical solutions for 114 uniformly-pressurized tri-axial ellipsoids involving a wide range of parameters (see Table A1 in Appendix E). We calculate the surface displacements and volume changes associated with the triaxial cavities by using the Nikkhoo & Walter (2015) half-space solution for Triangular Dislocations (TDs; see also Yoffe 1960; Comninou & Dundurs 1975) in a numerical scheme based on the Boundary Element Method (BEM; see Crouch 1976; Crouch & Starfield 1983; Kuriyama & Mizuta 1993). We illustrate the surface displacements associated with two representative cases (see Fig. 3). For the vertically elongated cavity, we find that, except for the vertical displacements right above the ellipsoid, the finite ECM and BEM solutions are nearly identical (Fig. 3a,b). The agreement is best along the y-axis, which is parallel to the semi-minor axis. For the second source, which is sill-like, the agreement is not as good (Fig. 3c,d). However, the functional shape of the solutions is very similar: indeed, a substantially better agreement is achieved if the displacements are normalized by method II (Fig. 3c,d). This implies that applying the finite ECM and Yang et al. (1988) solution (the Cervelli 2013, code) to source inversions involving sill-like sources may lead to fairly good constraints on the source shape, but the volume change and depth of the source may be biased considerably.

We further perform a systematic comparison between the finite ECM and BEM surface displace-

ments and volume changes for the 114 triaxial ellipsoids (see Table A1 in Appendix E). For these ellipsoids we calculate the volume change, δV, the horizontal and vertical surface displacements along the x axis, (u_x^h, u_x^v), and those along the y axis, (u_y^h, u_y^v). The relative volume change misfit is calculated as

$$\epsilon_{\delta V} = \frac{|\delta V(\text{fECM}) - \delta V(\text{BEM})|}{\delta V(\text{BEM})}, \tag{9}$$

where "fECM" and "BEM" refer to the finite ECM and BEM calculations, respectively. Also, we use

$$\epsilon_x^h = \frac{\int_0^{3dc} \left| u_x^h(fECM) - u_x^h(BEM) \right| dx}{\int_0^{3dc} |u_x^h(BEM)| dx}, \tag{10}$$

as a measure of misfit between $u_x^h(fECM)$ and $u_x^h(BEM)$. Similarly, we calculate ϵ_x^v, ϵ_y^h and ϵ_y^v as misfits between the finite ECM and BEM displacement components u_x^v, u_y^h and u_y^v, respectively. We define

$$\epsilon^h = \frac{\epsilon_x^h + \epsilon_y^h}{2},$$
$$\epsilon^v = \frac{\epsilon_x^v + \epsilon_y^v}{2}, \tag{11}$$

as the mean horizontal and mean vertical misfits. We calculate such misfit for displacements normalized by both method I and method II as ϵ_I^h, ϵ_I^v, ϵ_{II}^h and ϵ_{II}^v. To determine the range of applicability of the finite ECM we evaluate the mean horizontal and vertical misfits as a function of d_C/a_C, d_T/a_C, d_T/ρ_T^{max} and d_T/ρ_T^{min} (see Table A1). The results show that

1. d_T/ρ_T^{max} and d_T/ρ_T^{min} are only useful for vertical prolate sources as they misevaluate oblate and triaxial sources and also, rotated prolate sources.

2. the misfits ϵ_I^h and ϵ_I^v are below 10% and 15% for $d_C/a_C \gtrsim 1.75$ and $d_C/a_C \gtrsim 1.25$, respectively.

3. the misfits ϵ_{II}^h and ϵ_{II}^v are below 7% and 15% for $d_T/a_C \gtrsim 0.7$ and $d_T/a_C \gtrsim 0.5$, respectively.

4. $\epsilon_{\delta V}$ is smaller than 10% and 5% for $d_C/a_C \gtrsim 1.75$ and $d_C/a_C \gtrsim 2.5$, respectively. The largest $\epsilon_{\delta V}$ values correspond to shallow oblate ellipsoids. For very shallow oblate cavities $\epsilon_{\delta V}$ may become extremely large, occasionally even exceeding 100% (see "D0", "P0", "P1", "Q0" and "Q1" cases in Table A1).

Note that the criteria based on d_C/a_C and d_T/a_C are in agreement with the Amoruso et al. (2007) criterion, $d_C/a_C \gtrsim 0.8$, for penny-shaped cracks.

The d_T/ρ_T^{max} for the cavities in Fig. 2a-d are 1.8, 0.053, 0.8 and 0, respectively; the d_C/a_C are 1.2, 1, 1.8 and 1, respectively; and the d_T/a_C are 0.2, 0.94, 0.8 and 1, respectively. Thus, all these cavities satisfy at least one of the criteria listed above: the cavity in Fig. 2a satisfies $d_T/\rho_T^{max} \gtrsim 1$, the cavity in Fig. 2b satisfies the criteria based on d_C/a_C and d_T/a_C, the cavity in Fig. 2c satisfies the criteria

based on $d_\mathrm{T}/\rho_\mathrm{T}^\mathrm{max}$, $d_\mathrm{C}/a_\mathrm{C}$ and $d_\mathrm{T}/a_\mathrm{C}$, and the cavity in Fig. 2d satisfies the criteria based on $d_\mathrm{C}/a_\mathrm{C}$ and $d_\mathrm{T}/a_\mathrm{C}$.

The comparisons above show that the finite ECM is a reliable model for shallow triaxial sources, beyond what previously published solutions offer.

4   DISCUSSION

4.1   The approximations involved in the finite ECM and the other solutions

We developed the finite ECM in the form of distributed point CDMs having depth-dependent strengths but the same aspect ratio determined through the Eshelby (1957) shape functions (eq. 1). Unless the cavity shape is spherical, spheroidal or crack-like, these functions involve elliptic integrals, which can be calculated only numerically. All other components of the finite ECM—all steps of the adaptive algorithm controlling the configuration of the solution—are analytical.

Distributed point sources have been proposed in earlier works as a straightforward approach to simulate the near field deformations caused by shallow pressurized cavities with non-negligible characteristic dimension in comparison with the cavity depth (see Davis 1986; Wang et al. 2018). Amoruso et al. (2007) used a uniform distribution of point sources (Wang et al. 2006, semi-analytical solution) to simulate the surface displacements associated with a horizontal penny-shaped crack in a layered half-space, and applied it to the 2004–2006 uplift period at Campi Flegrei caldera. Also, Amoruso et al. (2008) used a similar approach for the joint inversion of surface displacements and gravity changes recorded during the 1982–1984 unrest period at Campi Flegrei. The finite ECM can facilitate similar inversions for generic ellipsoidal geometries.

The calibration and systematic comparisons between the finite ECM and the Yang et al. (1988) solution for a few thousand prolate and oblate cavities show that for $c_\mathrm{r}^* \geqslant 14$ the mismatch between the surface displacements from the two models are $\lesssim 1\%$ (Table 1). For most rapid source inversions, $c_\mathrm{r}^* = 10$ may be optimal, as it provides acceptable accuracy for reasonably short computation times. If it is clear from preliminary inversions (e.g. using the point CDM) that the source is prolate, smaller values for c_r^* may be sufficient. In any case, starting an inversion with the point CDM, before switching to the finite ECM first with $c_\mathrm{r}^* = 10$ and then higher c_r^*s for more limited parameter space may be a good procedure to follow.

Compared with the finite ECM, the Amoruso & Crescentini (2011) and Amoruso & Crescentini (2013) models require shorter computation times and thus, could potentially be useful for rapid source inversions. However, this demands a rigorous assessment of the range of applicability of these models. This is especially necessary regarding shallow oblate sources, for which the displacement patterns

from the Amoruso & Crescentini (2011) and Amoruso & Crescentini (2013) models may perform worse than point source solutions such as the Davis (1986) or the point CDM (Fig. 2b,d).

The fluctuations of the Amoruso & Crescentini (2011) and Amoruso & Crescentini (2013) models for shallow oblate sources, together with the interesting observation that the 7-point-source solution, at least in those cases from Fig 2, performs better than the Amoruso & Crescentini (2013) model call for an explanation. To understand the reason for this, it is important to note that, although both the Amoruso & Crescentini (2011) and Amoruso & Crescentini (2013) models are based on the same "quadrupole approximation", there are inherent differences between the two models. The Amoruso & Crescentini (2013) model is in fact a higher-order point-source model—it represents a special case of a rank-4 moment tensor. On the other hand, the Amoruso & Crescentini (2011) model is formed as the superposition of 7 rank-2 moment tensors of both positive and negative sign, distributed within the cavity. This distributed configuration gives the source some "finiteness", which might be what makes the 7-point-source model perform better, at least in the examined cases, than a rank-4 moment tensor. In the far field, these models reduce to a rank-2 moment tensor, but for oblate sources in the near field this fails to happen.

Among analytical volcano deformation sources, the McTigue (1987) and Fialko et al. (2001) solutions fulfil very accurately (although still not exactly) the uniform-pressure boundary conditions on the source walls. All the other available analytical source models, including Sun (1969); Yang et al. (1988); Amoruso & Crescentini (2011, 2013) and the finite ECM, make use of the Davis approximation. Therefore, inferring the parameters of uniformly pressurized magma bodies by using the latter group of source models may come with a substantial bias if the source is very shallow. Examples of this can be seen in Fig. 3a-d, where a perfect fit is achieved for oblate sources, but with a biased volume change. As also shown by Amoruso & Crescentini (2011), such a bias is likely to emerge on depth and source aspect ratio, beside volume change. Similarly, biases on the spatial orientation of the source could be expected. The extent of these biases as a function of source depth and shape has not been thoroughly investigated yet and should be addressed by future studies.

Our results concerning the normalization method I and method II, which we used in section 3, have direct implications for forward and inverse modelling using the finite ECM or any other source model involving the Davis approximation. Suppose that the surface displacements associated with a given pressurized cavity are calculated by using two different source models: an accurate model and an approximate model. Applying the normalization method I preserves the relative misfit between the displacements from the two models—this misfit reflects the actual accuracy (or error) associated with the approximate model for a given set of parameters. Evaluating this misfit is important when using the approximate model for forward modelling purposes (e.g. analyzing the synthetic displacements

expected for a certain cavity). On the other hand, applying normalization method II scales the displacements such that the maximum vertical displacements from the two models become equal to 1. This leads to overall smaller misfits for the normalized displacements. The implication is that the approximate model may lead to an acceptable, or even an excellent, fit when used for inverse modelling of actual deformation data measured in the field. A significant difference between the misfits from normalization method I and those from normalization method II imply that, in an inversion using the approximate source, the source strength (volume change), and possibly other source parameters, may be misestimated.

4.2   The added value of triaxial finite-source solutions

The deformation signals measured at the Earth's surface can be used to infer some large-scale features of pressurized magma chambers. These large-scale features are in fact the deformation source parameters, which can be constrained through deformation modelling. For deep sources, these parameters are limited to the location, spatial orientation and strength; in this case point-source and finite-source models yield the same results. For shallow sources, in addition to the location, spatial orientation and strength, it is possible to constrain the source dimensions, provided that displacement data in the near-field are available. Finite triaxial sources help better constrain the aspect ratio and size, and thus, the volume of pressurized magma bodies. This would be of great benefit, as the overall volume of magma reservoirs is a poorly constrained quantity in volcanology. In this case, point-source solutions cannot be used because they cannot represent the displacements in the near field. Therefore, to infer the parameters of shallow magma chambers correctly, finite-source models need to be used.

It is difficult to estimate how often a triaxial finite source can be applied. So far, triaxial point sources were applied to study the geometry of magma storage at Kilauea volcano (Davis 1986) and Long Valley caldera(Langbein et al. 1995), to constrain a draining magma reservoir at Calbuco volcano (Nikkhoo et al. 2017), offshore Mayotte (Cesca et al. 2020) and Erta Ale volcano (Xu et al. 2020), and to track magma ascent at Piton de la Fournaise (Beauducel et al. 2020b). A finite triaxial source may help better explore some of these cases, or constrain other unexplored cases involving shallow sources.

In standard inversion procedures, different analytical solutions are tested one by one searching for an optimal match with observations. Nikkhoo et al. (2017), Beauducel et al. (2020b) and Peltier et al. (2020) showed the benefit of avoiding such one-by-one matching and relying on the ability of the point CDM to span the entire model space with just one model. By feeding the data into such an automatic procedure, it is possible to reveal the underlying cause of the deformation, be it the (de)pressurization of an equi-dimensional body such as a reservoir (Cesca et al. 2020; Xu et al. 2020), or the propagation

of a dike (Sigmundsson et al. 2015; Xu et al. 2016; Dumont et al. 2018; Beauducel et al. 2020b; Peltier et al. 2020; Davis et al. 2021). The finite ECM extends this capability to deformation sources in the near field.

4.3 The volume change and the compressibility associated with the finite ECM

In order to fully characterize a volcano deformation source, it is critical to provide the practical means to calculate the volume change upon pressurization. The volume change is a measure of the source strength and can be used to estimate other important quantities such as the chamber compressibility, defined as the relative volume change for a unit pressurization. The chamber compressibility, together with the magma compressibility, is critical to estimate the real intrusion volume.

The volume change associated with ellipsoidal sources in a full space can be calculated from the Eshelby (1957) solution (see Amoruso & Crescentini 2009, 2013). This "full-space" volume change is also used as an approximation for the half-space models. This is because the exact volume change in half-space source models cannot be calculated analytically. One caveat is that the volume change for shallow sources in a half-space may be substantially different from the full-space volume change—accurate half-space volume change calculations require numerical methods (see Amoruso & Crescentini 2009; Anderson & Segall 2011). Since volume change and chamber compressibility may be important magma chamber properties both for inversions and for forward modelling of eruptive volumes (Mastin et al. 2008; Anderson & Segall 2011; Wasser et al. 2021), we include codes based on the Eshelby (1957) approach for the accurate calculation of the full-space volume change and chamber compressibility (see Segall et al. 2001; Rivalta & Segall 2008; Segall 2010).

4.4 Implications for modelling deformation-induced gravity changes

Okubo (1991) developed an analytical solution for surface gravity changes caused by point dislocations. Based on Okubo (1991)'s work, Nikkhoo & Rivalta (2022) developed an analytical solution for deformation-induced gravity changes associated with the point CDM. We use the Nikkhoo & Rivalta (2022) point-source solution for gravity changes within the adaptive algorithm in section 2.1 to develop the gravity change solution associated with the finite ECM.

A major contribution to the surface gravity changes caused by any deformation source is due to the source volume change (e.g., Okubo 1991; Nikkhoo & Rivalta 2022). Considering that the estimated volume change for the finite ECM may be subject to large biases (see section 3), caution is advised while applying the finite ECM to joint inversions of surface deformations and gravity changes.

5   CONCLUSIONS

1. We developed a computationally-efficient solution for the surface deformation field caused by a finite triaxial ellipsoidal source in the form of a non-uniform (depth-dependent) distribution of point CDMs. The finite ECM is especially suitable for inversions of surface deformation data.

2. The finite ECM includes an adaptive algorithm that determines the optimal spacing and location of the point CDMs as a function of the depth, shape, and spatial orientation of the cavity, and a grid-spacing parameter c_r^*.

3. We showed that the Yang et al. (1988) solution can be used to benchmark the finite ECM and calibrate c_r^*, or alternatively N_{max}, to achieve any desired accuracy while maintaining computation time minimal. We further validated the finite ECM through comparisons with other analytical and numerical solutions.

4. Through comparisons with numerical solutions we found new empirical criteria for the accuracy of the finite ECM calculations. As rules of thumb, a finite ECM with $d_C/a_C \gtrsim 2$ yields excellent results—this criterion is especially useful for forward modelling of the surface displacements; a finite ECM with $d_T/a_C \gtrsim 1$ performs very well in source inversions, with the caveat that some parameters (especially volume change and depth) may be biased. Our results show that the Yang et al. (1988) criterion ($d_T \gtrsim \rho_T$) is only appropriate for vertical prolate spheroids and cannot be extended to triaxial ellipsoids.

5. We provide MATLAB codes for the finite ECM (surface displacements and deformation-induced gravity changes) and additional codes to calculate the volume change and chamber compressibility of ellipsoidal sources. The codes do not contain any MATLAB-specific function and it is straightforward to convert them to any other programming language.

DATA AVAILABILITY

The MATLAB codes will be provided at http://www.volcanodeformation.com/ upon acceptance.

APPENDIX A: ANALYTICAL SOLUTIONS FOR THE SHALLOWEST AND DEEPEST POINTS ON THE SURFACE OF A GENERIC ELLIPSOID

The standard ellipsoid E_S centered at the origin of a Cartesian xyz coordinate system has the form

$$\frac{x^2}{a_x^2} + \frac{y^2}{a_y^2} + \frac{z^2}{a_z^2} = 1, \tag{A.1}$$

where the semi-axes a_x, a_y and a_z are aligned with the x, y and z coordinate axes, respectively. If (θ, λ) denote the spherical coordinates, of an arbitrary point P on the surface of E_S, we have

$$x = a_x \sin\theta \cos\lambda,$$

$$y = a_y \sin\theta \sin\lambda,$$

$$z = a_z \cos\theta, \tag{A.2}$$

where $\theta \in [0, \pi]$ and $\lambda \in [0, 2\pi)$. The matrices

$$R_x(\omega_x) = \begin{pmatrix} 1 & 0 & 0 \\ 0 & \cos\omega_x & \sin\omega_x \\ 0 & -\sin\omega_x & \cos\omega_x \end{pmatrix}$$

$$R_y(\omega_y) = \begin{pmatrix} \cos\omega_y & 0 & -\sin\omega_y \\ 0 & 1 & 0 \\ \sin\omega_y & 0 & \cos\omega_y \end{pmatrix},$$

$$R_z(\omega_z) = \begin{pmatrix} \cos\omega_z & \sin\omega_z & 0 \\ -\sin\omega_z & \cos\omega_z & 0 \\ 0 & 0 & 1 \end{pmatrix}, \tag{A.3}$$

represent general rotations about the x, y and z axes, respectively. Any arbitrary rotation in xyz can be represented in the form of

$$R = R_x(\omega_x) R_y(\omega_y) R_z(\omega_z) = \begin{pmatrix} r_{11} & r_{12} & r_{13} \\ r_{21} & r_{22} & r_{23} \\ r_{31} & r_{32} & r_{33} \end{pmatrix}, \tag{A.4}$$

with a unique set of angles $(\omega_x, \omega_y, \omega_z)$. After applying such a rotation, the new coordinates of P are

$$\begin{pmatrix} x' \\ y' \\ z' \end{pmatrix} = \begin{pmatrix} r_{11} & r_{12} & r_{13} \\ r_{21} & r_{22} & r_{23} \\ r_{31} & r_{32} & r_{33} \end{pmatrix} \begin{pmatrix} x \\ y \\ z \end{pmatrix}. \tag{A.5}$$

Combining equations A.5 and A.2 yields

$$z' = r_{31}a_x \sin\theta \cos\lambda + r_{32}a_y \sin\theta \sin\lambda + r_{33}a_z \cos\theta. \tag{A.6}$$

The spherical coordinates of the two points with the minimum and maximum z values on the ellipsoid are the solutions of the equation

$$\frac{\partial z'}{\partial \lambda} = 0, \quad \frac{\partial z'}{\partial \theta} = 0, \tag{A.7}$$

that can be written in explicit form as

$$\lambda = \operatorname{atan}\left(\frac{r_{32}a_y}{r_{31}a_x}\right), \quad \theta = \operatorname{atan}\left(\frac{\sqrt{r_{31}^2 a_x^2 + r_{32}^2 a_y^2}}{r_{33}a_z}\right). \tag{A.8}$$

APPENDIX B: AN ANALYTICAL EXPRESSION FOR THE VOLUME OF A PARTITION OF AN ELLIPSOID BOUNDED BY TWO HORIZONTAL PLANES

Let C_{P} denote the ellipsoidal cap formed by the intersection of the standard ellipsoid, E_{S} (equation A.1) and an arbitrary plane, $S : Ax + By + Cz = D$, where the vector (A, B, C) is normal to the plane and points towards C_{P}. The volume of C_{P} is

$$V_{\mathrm{P}}(S) = \iiint_{C_{\mathrm{P}}} dx\,dy\,dz. \tag{B.1}$$

In a new Cartesian XYZ coordinate system, where $x = a_x X$, $y = a_y Y$ and $z = a_z Z$ the ellipsoid is mapped onto the unit sphere, $X^2 + Y^2 + Z^2 = 1$, and the plane is mapped onto the new plane $S' : Aa_x X + Ba_y Y + Ca_z Z = D$. Also, equation B.1 can be rewritten as

$$V_{\mathrm{P}}(S) = V_{\mathrm{P}}(S') = a_x a_y a_z \iiint_{C'_{\mathrm{P}}} dX\,dY\,dZ, \tag{B.2}$$

where

$$\iiint_{C'_{\mathrm{P}}} dX\,dY\,dZ = \frac{1}{3}\pi(1 - d_{\mathrm{n}})^2(2 + d_{\mathrm{n}}), \tag{B.3}$$

is the volume of the spherical cap, C'_{P}, that is bounded by the unit sphere and the new plane (see Kern & Bland 1938, p. 37 and Harris & Stöcker 1998, p. 107) and $d_{\mathrm{n}} = D/(A^2 a_x^2 + B^2 a_y^2 + C^2 a_z^2)^{1/2}$ is the shortest distance from the origin of XYZ to the new plane. Substituting equation B.3 in equation B.2 yields:

$$V_{\mathrm{P}}(S) = \frac{1}{3}\pi a_x a_y a_z (1 - d_{\mathrm{n}})^2(2 + d_{\mathrm{n}}). \tag{B.4}$$

Thus, the volume of the region inside E_{S} and bounded by two parallel planes $S_1 : Ax + By + Cz = D_1$ and $S_2 : Ax + By + Cz = D_2$ can be calculated as

$$V_{D_1 D_2} = |V_{\mathrm{P}}(S_2) - V_{\mathrm{P}}(S_1)|. \tag{B.5}$$

569 For an arbitrary ellipsoid subjected to the rotations $R_x(\omega_x)R_y(\omega_y)R_z(\omega_z)$ and centered at $(x_0, y_0, -d)$,

570 the volume of the region inside the ellipsoid and bounded by two horizontal planes $z = z_1$ and

571 $z = z_2$ can be calculated from equation B.5 after applying the translation $(-x_0, -y_0, d)$ and rotations

572 $R_z(-\omega_z)R_y(-\omega_y)R_x(-\omega_x)$ to the ellipsoid and both planes.

573 **APPENDIX C: INTERSECTION OF A PLANE AND AN ARBITRARY ELLIPSOID**

574 In order to determine the intersection ellipse associated with a horizontal plane, $S_\mathrm{H} : z = z_j$, and an

575 arbitrary ellipsoid E_R subjected to the rotations $R_x(\omega_x)R_y(\omega_y)R_z(\omega_z)$ and centered at $(x_0, y_0, -d)$,

576 we first apply the translation $(-x_0, -y_0, d)$ and rotations $R_z(-\omega_z)R_y(-\omega_y)R_x(-\omega_x)$ to both E_R and

577 S_H. These transformations lead to a standard ellipsoid E_S (equation A.1, and a plane of the form

578 $S : Ax + By + Cz = D$. The intersection ellipse formed by E_S and S can be determined through the

579 Klein (2012) formulas. Applying the rotations $R_x(\omega_x)R_y(\omega_y)R_z(\omega_z)$ and the translation $(x_0, y_0, -d)$

580 to the ellipse from the previous step yields the solution.

581 **APPENDIX D: PRINCIPAL CURVATURES AT ANY POINT ON THE SURFACE OF AN**

582 **ELLIPSOID**

583 The principal curvatures, κ_max and κ_min, at any point $P(\theta, \lambda)$ on the surface of the standard ellipsoid

584 (equation A.1) are the solutions of the following equation:

585
$$(EG - F^2)\kappa^2 - (EN + GL - 2FM)\kappa + (LN - M^2) = 0, \tag{D.1}$$

586 where E, F and G are the first fundamental coefficients and L, M and N are the second fundamental

587 coefficients of the ellipsoid (see Lipschutz 1969, p. 183). A simplified form of equation D.1 can be

588 written as

589
$$A\kappa^2 + B\kappa + C = 0, \tag{D.2}$$

where

$$
\begin{aligned}
A = (&a_x^2 \cos^2 \theta \cos^2 \lambda + a_y^2 \cos^2 \theta \sin^2 \lambda \\
&+ a_z^2 \sin^2 \theta)(a_x^2 \sin^2 \lambda + a_y^2 \cos^2 \lambda) \\
&- (a_y^2 - a_x^2)^2 \cos^2 \theta \sin^2 \lambda \cos^2 \lambda,
\end{aligned}
$$

$$
\begin{aligned}
B = \frac{-a_x a_y a_z}{q_n}(&a_x^2 \cos^2 \theta \cos^2 \lambda + a_y^2 \cos^2 \theta \sin^2 \lambda \\
&+ a_z^2 \sin^2 \theta + a_x^2 \sin^2 \lambda + a_y^2 \cos^2 \lambda),
\end{aligned}
$$

$$
C = (a_x a_y a_z / q_n)^2, \tag{D.3}
$$

in which

$$
q_n = (a_y^2 a_z^2 \sin^2 \theta \cos^2 \lambda + a_x^2 a_z^2 \sin^2 \theta \sin^2 \lambda + a_x^2 a_y^2 \cos^2 \theta)^{1/2}.
$$

A singularity in equation D.1 at $\theta = 0$ has been addressed analytically in equation D.2. The maximum and minimum radii of curvature at P are

$$
\rho_{\max} = 1/\kappa_{\min}, \quad \rho_{\min} = 1/\kappa_{\max}. \tag{D.4}
$$

APPENDIX E: COMPARISONS USING THE BEM SOLUTIONS

We compared the surface displacements and volume changes calculated from the finite ECM and BEM for 114 triaxial ellipsoidal cavities (see Table A1). The number of TDs forming the cavities (except "Y1" and "Y2", last two lines in Table A1) varies between 792 and 1984, with an average of 1138; the shallower and larger cavities possess more TDs. The cavity mesh in the "Y1" and "Y2" models is composed of 2456 and 4092 TDs, respectively—these models represent the same source and were used for a convergence test. Based on similar tests, we estimate a relative error of up to a few per cent for both the surface displacements and volume changes calculated using the BEM.

Table A1: Numerical benchmarking of the finite ECM using the BEM solutions. The semiaxes, a_x, a_y, a_z, and depth, d_C, of the cavities have the same arbitrary unit; the rotation angles, ω_x and ω_y, are given in degrees. The mean horizontal and vertical misfits associated with normalization method I, ϵ_I^h and ϵ_I^v, respectively, and those associated with method II, ϵ_{II}^h, ϵ_{II}^v, and also the relative volume change misfit, $\epsilon_{\delta V}$, are given in per cent (see section 3).

#	a_x	a_y	a_z	d_C	ω_x	ω_y	ϵ_I^h	ϵ_I^v	ϵ_{II}^h	ϵ_{II}^v	$\epsilon_{\delta V}$	$\frac{d_C}{a_C}$	$\frac{d_T}{a_C}$	$\frac{d_T}{\rho_{\max}}$	$\frac{d_T}{\rho_{\min}}$
A1	0.6	0.4	1.2	1.5	0	0	7.7	11	9.9	7.4	7.8	1.25	0.25	1	2.25
A2	0.6	0.4	1.2	1.8	0	0	6.0	7.8	3.8	3.6	6.3	1.5	0.5	2	4.5

Continuation of Table A1

#	a_x	a_y	a_z	d_C	ω_x	ω_y	ϵ_H^I	ϵ_V^I	ϵ_H^{II}	ϵ_V^{II}	$\epsilon_{\delta V}$	$\frac{d_C}{a_C}$	$\frac{d_T}{a_C}$	$\frac{d_T}{\rho_{max}}$	$\frac{d_T}{\rho_{min}}$
A3	0.6	0.4	1.2	2.4	0	0	5.2	6.2	3.2	2.7	5.4	2.0	1.0	4	9
A4	0.6	0.4	1.2	3.0	0	0	5.0	5.7	3.2	2.6	5.1	2.5	1.5	6	14
A5	0.6	0.4	1.2	3.6	0	0	4.8	5.5	3.2	2.5	5.0	3.0	2.0	8	18
B1	0.3	0.2	1.2	1.5	0	0	6.2	7.1	4.1	3.5	5.4	1.25	0.25	4	9
B2	0.3	0.2	1.2	1.8	0	0	5.8	6.4	4.2	3.4	5.1	1.5	0.5	8	18
B3	0.3	0.2	1.2	2.4	0	0	5.6	6.0	4.2	3.4	4.8	2.0	1.0	16	36
B4	0.3	0.2	1.2	3.0	0	0	5.6	6.0	4.2	3.5	4.8	2.5	1.5	24	54
B5	0.3	0.2	1.2	3.6	0	0	5.5	5.9	4.2	3.4	4.8	3.0	2.0	32	72
C1	0.1	1.2	1.2	1.5	0	0	9.8	12	1.9	4.6	8.4	1.25	0.25	0.25	36
C2	0.1	1.2	1.2	1.8	0	0	6.0	7.9	1.3	3.3	6.1	1.5	0.5	0.5	72
C3	0.1	1.2	1.2	2.4	0	0	4.0	5.9	1.1	2.7	4.5	2.0	1.0	1	140
C4	0.1	1.2	1.2	3.0	0	0	3.3	5.2	1.0	2.6	4.0	2.5	1.5	1.5	220
C5	0.1	1.2	1.2	3.6	0	0	3.2	5.1	1.1	2.4	3.8	3.0	2.0	2	290
D0	1.5	1.2	0.1	0.9	0	0	45	46	11	7.3	77	0.6	0.53	0.036	0.056
D1	1.5	1.2	0.1	1.5	0	0	20	21	2.3	1.3	25	1.0	0.93	0.062	0.097
D2	1.5	1.2	0.1	1.8	0	0	14	15	1.2	0.6	17	1.2	1.1	0.076	0.12
D3	1.5	1.2	0.1	2.4	0	0	8.1	8.3	0.5	0.3	9.2	1.6	1.5	0.10	0.16
D4	1.5	1.2	0.1	3.0	0	0	5.0	5.2	0.4	0.2	5.9	2.0	1.9	0.13	0.20
D5	1.5	1.2	0.1	3.6	0	0	3.7	3.8	0.4	0.1	4.3	2.4	2.3	0.16	0.24
J0	1.5	0.3	0.3	0.9	0	0	9.4	12	7.1	4.1	11	0.6	0.4	0.08	2
J1	1.5	0.3	0.3	1.2	0	0	6.5	7.5	3.4	2.0	8.0	0.8	0.6	0.12	3
J2	1.5	0.3	0.3	1.5	0	0	5.0	5.5	1.6	1.0	6.6	1.0	0.8	0.16	4
J3	1.5	0.3	0.3	1.8	0	0	4.2	4.4	0.9	0.5	5.9	1.2	1.0	0.20	5
J5	1.5	0.3	0.3	2.4	0	0	3.5	3.5	0.7	0.2	5.3	1.6	1.4	0.28	7
J6	1.5	0.3	0.3	2.7	0	0	3.3	3.2	0.6	0.3	5.2	1.8	1.6	0.32	8
J7	1.5	0.3	0.3	3.0	0	0	3.0	3.0	0.6	0.3	5.1	2.0	1.8	0.36	9
K1	0.6	0.4	1.2	1.5	0	-10	7.7	11	10	7.3	7.8	1.3	0.26	1.0	2.3
K2	0.6	0.4	1.2	1.5	0	-20	7.6	11	11	7.3	7.8	1.3	0.29	1.0	2.5
K3	0.6	0.4	1.2	1.5	0	-30	7.8	11	11	7.2	7.7	1.3	0.35	1.0	2.8
K4	0.6	0.4	1.2	1.5	0	-40	7.9	11	10	6.4	7.7	1.3	0.42	0.96	3.1
K5	0.6	0.4	1.2	1.5	0	-50	8.0	11	8.7	5.5	7.7	1.3	0.50	0.84	3.4
K6	0.6	0.4	1.2	1.5	0	-60	8.1	10	7.9	5.0	7.7	1.3	0.59	0.68	3.5

Continuation of Table A1

#	a_x	a_y	a_z	d_C	ω_x	ω_y	ϵ_H^{I}	ϵ_V^{I}	ϵ_H^{II}	ϵ_V^{II}	$\epsilon_{\delta V}$	$\frac{d_C}{a_C}$	$\frac{d_T}{a_C}$	$\frac{d_T}{\rho_{\max}}$	$\frac{d_T}{\rho_{\min}}$
K7	0.6	0.4	1.2	1.5	0	-70	7.9	9.9	7.0	4.5	7.7	1.3	0.67	0.53	3.5
K8	0.6	0.4	1.2	1.5	0	-80	7.9	9.7	6.9	4.5	7.7	1.3	0.73	0.41	3.4
K9	0.6	0.4	1.2	1.5	0	-90	7.7	9.5	6.7	4.5	7.7	1.3	0.75	0.38	3.4
L1	0.6	0.4	1.2	1.5	-10	0	8.0	11	8.1	6.1	8.0	1.3	0.26	1.0	2.3
L2	0.6	0.4	1.2	1.5	-20	0	8.0	10	7.3	5.2	8.3	1.3	0.30	1.2	2.3
L3	0.6	0.4	1.2	1.5	-30	0	7.9	9.8	6.5	4.6	8.9	1.3	0.37	1.3	2.3
L4	0.6	0.4	1.2	1.5	-40	0	7.8	9.5	5.9	4.1	9.5	1.3	0.46	1.5	2.1
L5	0.6	0.4	1.2	1.5	-50	0	7.7	9.1	5.2	3.5	10	1.3	0.56	1.5	1.7
L6	0.6	0.4	1.2	1.5	-60	0	7.5	8.9	4.3	2.8	11	1.3	0.67	1.2	1.6
L7	0.6	0.4	1.2	1.5	-70	0	7.6	8.8	3.9	2.5	11	1.3	0.79	0.71	1.5
L8	0.6	0.4	1.2	1.5	-80	0	7.7	8.9	3.5	2.1	11	1.3	0.88	0.41	1.3
L9	0.6	0.4	1.2	1.5	-90	0	7.7	8.9	2.9	1.5	11	1.3	0.92	0.31	1.2
M1	0.6	0.4	1.2	1.8	0	-10	6.1	7.9	4.1	3.8	6.3	1.5	0.51	2.0	4.6
M2	0.6	0.4	1.2	1.8	0	-20	6.3	8.1	4.5	3.9	6.3	1.5	0.55	1.9	4.7
M3	0.6	0.4	1.2	1.8	0	-30	6.5	8.1	5.1	3.9	6.3	1.5	0.60	1.8	4.9
M4	0.6	0.4	1.2	1.8	0	-40	6.7	8.1	5.7	4.0	6.4	1.5	0.67	1.5	5.0
M5	0.6	0.4	1.2	1.8	0	-50	6.9	8.1	5.7	3.9	6.4	1.5	0.75	1.3	5.1
M6	0.6	0.4	1.2	1.8	0	-60	6.9	8.0	5.2	3.5	6.4	1.5	0.84	0.97	5.0
M7	0.6	0.4	1.2	1.8	0	-70	6.8	7.9	4.9	3.3	6.5	1.5	0.92	0.72	4.8
M8	0.6	0.4	1.2	1.8	0	-80	6.5	7.6	4.3	2.9	6.5	1.5	0.98	0.56	4.6
M9	0.6	0.4	1.2	1.8	0	-90	6.3	7.5	4.3	2.9	6.5	1.5	1.0	0.5	4.5
N1	0.6	0.4	1.2	1.8	-10	0	6.0	7.3	3.3	3.1	6.4	1.5	0.51	2.0	4.4
N2	0.6	0.4	1.2	1.8	-20	0	5.8	6.8	2.8	2.4	6.6	1.5	0.55	2.1	4.2
N3	0.6	0.4	1.2	1.8	-30	0	5.5	6.4	2.5	1.9	7.0	1.5	0.62	2.2	3.8
N4	0.6	0.4	1.2	1.8	-40	0	5.4	6.2	2.5	1.8	7.4	1.5	0.71	2.2	3.2
N5	0.6	0.4	1.2	1.8	-50	0	5.2	5.9	2.2	1.5	7.9	1.5	0.81	2.2	2.4
N6	0.6	0.4	1.2	1.8	-60	0	5.2	5.9	2.0	1.3	8.2	1.5	0.92	1.6	2.1
N7	0.6	0.4	1.2	1.8	-70	0	5.1	5.7	1.6	0.9	8.5	1.5	1.04	0.93	1.9
N8	0.6	0.4	1.2	1.8	-80	0	5.4	5.9	1.4	0.8	8.7	1.5	1.13	0.52	1.7
N9	0.6	0.4	1.2	1.8	-90	0	5.6	6.0	1.2	0.7	8.8	1.5	1.17	0.39	1.6
O1	0.6	0.4	1.2	2.1	-10	0	5.2	6.1	3.0	2.6	5.7	1.8	0.76	3.0	6.6
O2	0.6	0.4	1.2	2.1	-20	0	4.8	5.4	2.5	2.0	5.9	1.8	0.80	3.0	6.1

Continuation of Table A1

#	a_x	a_y	a_z	d_C	ω_x	ω_y	ϵ_H^I	ϵ_V^I	ϵ_H^{II}	ϵ_V^{II}	$\epsilon_{\delta V}$	$\frac{d_C}{a_C}$	$\frac{d_T}{a_C}$	$\frac{d_T}{\rho_{max}}$	$\frac{d_T}{\rho_{min}}$
O3	0.6	0.4	1.2	2.1	-30	0	4.4	4.9	2.0	1.4	6.1	1.8	0.87	3.1	5.4
O4	0.6	0.4	1.2	2.1	-40	0	4.2	4.6	1.5	1.1	6.4	1.8	0.96	3.0	4.3
O5	0.6	0.4	1.2	2.1	-50	0	4.1	4.4	1.2	0.9	6.7	1.8	1.06	2.9	3.2
O6	0.6	0.4	1.2	2.1	-60	0	3.9	4.1	0.8	0.6	7.0	1.8	1.2	2.0	2.7
O7	0.6	0.4	1.2	2.1	-70	0	4.0	4.2	0.7	0.5	7.2	1.8	1.3	1.15	2.4
O8	0.6	0.4	1.2	2.1	-80	0	3.8	4.0	0.3	0.1	7.4	1.8	1.4	0.64	2.1
O9	0.6	0.4	1.2	2.1	-90	0	4.1	4.1	0.2	0.2	7.4	1.8	1.4	0.47	1.9
P0	1.5	1.5	0.1	0.9	0	0	52	53	14	8.9	100	0.6	0.53	0.036	0.036
P1	1.5	1.5	0.1	1.2	0	0	36	37	6.8	4.4	53	0.8	0.73	0.049	0.049
P2	1.5	1.5	0.1	1.5	0	0	25	25	3.2	2.0	33	1.0	0.93	0.062	0.062
P3	1.5	1.5	0.1	1.8	0	0	18	18	1.6	1.0	22	1.2	1.1	0.076	0.076
P4	1.5	1.5	0.1	2.1	0	0	13	13	0.6	0.4	16	1.4	1.3	0.089	0.089
P5	1.5	1.5	0.1	2.4	0	0	10	11	0.6	0.3	12	1.6	1.5	0.10	0.10
P6	1.5	1.5	0.1	2.7	0	0	7.8	8.0	0.4	0.2	9.3	1.8	1.7	0.12	0.12
P7	1.5	1.5	0.1	3	0	0	6.4	6.7	0.4	0.2	7.5	2.0	1.9	0.13	0.13
P8	1.5	1.5	0.1	3.3	0	0	4.9	5.2	0.8	0.6	6.3	2.2	2.1	0.14	0.14
P9	1.5	1.5	0.1	3.6	0	0	4.7	4.7	0.3	0.1	5.4	2.4	2.3	0.16	0.16
Q0	1.5	1.5	0.3	0.9	0	0	54	58	29	16	120	0.6	0.4	0.08	0.08
Q1	1.5	1.5	0.3	1.2	0	0	37	40	15	8.3	60	0.8	0.6	0.12	0.12
R1	0.6	0.4	1.2	2.1	0	-10	5.6	6.8	3.2	3.0	5.7	1.8	0.76	2.9	6.8
R2	0.6	0.4	1.2	2.1	0	-20	5.8	6.9	3.4	3.1	5.7	1.8	0.80	2.8	6.8
R3	0.6	0.4	1.2	2.1	0	-30	6.0	7.0	3.7	3.0	5.7	1.8	0.85	2.5	6.9
R4	0.6	0.4	1.2	2.1	0	-40	6.2	7.0	4.1	3.0	5.8	1.8	0.92	2.1	6.9
R5	0.6	0.4	1.2	2.1	0	-50	6.4	7.0	4.5	3.0	5.8	1.8	1.0	1.7	6.8
R6	0.6	0.4	1.2	2.1	0	-60	6.5	7.0	4.3	2.9	5.8	1.8	1.1	1.3	6.5
R7	0.6	0.4	1.2	2.1	0	-70	6.1	6.8	3.8	2.5	5.9	1.8	1.2	0.92	6.1
R8	0.6	0.4	1.2	2.1	0	-80	6.0	6.7	3.6	2.5	5.9	1.8	1.2	0.70	5.8
R9	0.6	0.4	1.2	2.1	0	-90	5.9	6.7	3.6	2.5	5.9	1.8	1.3	0.63	5.6
S1	0.6	0.4	1.2	2.4	0	-10	5.3	6.2	3.3	2.8	5.4	2.0	1.0	3.9	9.0
S2	0.6	0.4	1.2	2.4	0	-20	5.5	6.3	3.4	2.8	5.4	2.0	1.0	3.6	9.0
S3	0.6	0.4	1.2	2.4	0	-30	5.7	6.4	3.6	2.7	5.4	2.0	1.1	3.2	8.9
S4	0.6	0.4	1.2	2.4	0	-40	5.9	6.4	3.7	2.6	5.4	2.0	1.2	2.7	8.7

Continuation of Table A1

#	a_x	a_y	a_z	d_C	ω_x	ω_y	ϵ_H^{I}	ϵ_V^{I}	ϵ_H^{II}	ϵ_V^{II}	$\epsilon_{\delta V}$	$\frac{d_C}{a_C}$	$\frac{d_T}{a_C}$	$\frac{d_T}{\rho_{\max}}$	$\frac{d_T}{\rho_{\min}}$
S5	0.6	0.4	1.2	2.4	0	-50	6.0	6.4	3.9	2.5	5.5	2.0	1.3	2.1	8.4
S6	0.6	0.4	1.2	2.4	0	-60	6.1	6.4	3.8	2.5	5.5	2.0	1.3	1.6	8.0
S7	0.6	0.4	1.2	2.4	0	-70	6.1	6.4	3.6	2.5	5.5	2.0	1.4	1.1	7.4
S8	0.6	0.4	1.2	2.4	0	-80	5.5	6.1	3.3	2.1	5.5	2.0	1.5	0.84	6.9
S9	0.6	0.4	1.2	2.4	0	-90	5.3	5.9	3.1	1.9	5.5	2.0	1.5	0.75	6.8
T1	0.6	0.4	1.2	2.4	-10	0	4.8	5.5	3.0	2.5	5.4	2.0	1.0	4.0	8.8
T2	0.6	0.4	1.2	2.4	-20	0	4.3	4.6	2.6	1.9	5.5	2.0	1.1	4.0	8.0
T3	0.6	0.4	1.2	2.4	-30	0	3.8	4.0	2.1	1.4	5.7	2.0	1.2	3.9	6.9
T4	0.6	0.4	1.2	2.4	-40	0	3.5	3.6	1.6	1.0	5.9	2.0	1.2	3.8	5.5
T5	0.6	0.4	1.2	2.4	-50	0	3.3	3.4	1.2	0.8	6.1	2.0	1.3	3.6	3.9
T6	0.6	0.4	1.2	2.4	-60	0	3.4	3.4	0.9	0.6	6.3	2.0	1.4	2.5	3.3
T7	0.6	0.4	1.2	2.4	-70	0	3.0	3.0	0.6	0.4	6.5	2.0	1.5	1.4	2.9
T8	0.6	0.4	1.2	2.4	-80	0	3.1	3.0	0.5	0.2	6.6	2.0	1.6	0.75	2.4
T9	0.6	0.4	1.2	2.4	-90	0	3.3	3.0	0.8	0.4	6.6	2.0	1.7	0.56	2.2
Y1	0.2	0.2	1.2	3.6	0	0	3.5	4.4	1.4	1.4	4.8	3.0	2.0	72	72
Y2	0.2	0.2	1.2	3.6	0	0	3.0	3.8	1.3	1.3	3.7	3.0	2.0	72	72

REFERENCES

Amoruso, A. & Crescentini, L., 2009. Shape and volume change of pressurized ellipsoidal cavities from deformation and seismic data, *Journal of Geophysical Research: Solid Earth*, **114**(B2).

Amoruso, A. & Crescentini, L., 2011. Modelling deformation due to a pressurized ellipsoidal cavity, with reference to the campi flegrei caldera, italy, *Geophysical Research Letters*, **38**(1).

Amoruso, A. & Crescentini, L., 2013. Analytical models of volcanic ellipsoidal expansion sources, *Annals of Geophysics*, **56**(4), 0435.

Amoruso, A., Crescentini, L., Linde, A. T., Sacks, I. S., Scarpa, R., & Romano, P., 2007. A horizontal crack in a layered structure satisfies deformation for the 2004–2006 uplift of Campi Flegrei, *Geophysical Research Letters*, **34**(22).

Amoruso, A., Crescentini, L., & Berrino, G., 2008. Simultaneous inversion of deformation and gravity changes in a horizontally layered half-space: evidences for magma intrusion during the 1982–1984 unrest at Campi Flegrei caldera (Italy), *Earth and Planetary Science Letters*, **272**(1-2), 181–188.

Amoruso, A., Crescentini, L., & Sabbetta, I., 2014. Paired deformation sources of the Campi Flegrei caldera

(Italy) required by recent (1980-2010) deformation history, *Journal of Geophysical Research: Solid Earth*, **119**(2), 858–879.

Anderson, K. & Segall, P., 2011. Physics-based models of ground deformation and extrusion rate at effusively erupting volcanoes, *Journal of Geophysical Research: Solid Earth*, **116**(B7).

Anderson, K. & Segall, P., 2013. Bayesian inversion of data from effusive volcanic eruptions using physics-based models: Application to Mount St. Helens 2004–2008, *Journal of Geophysical Research: Solid Earth*, **118**(5), 2017–2037.

Anderson, K. R. & Poland, M. P., 2016. Bayesian estimation of magma supply, storage, and eruption rates using a multiphysical volcano model: Kīlauea volcano, 2000–2012, *Earth and Planetary Science Letters*, **447**, 161–171.

Bagnardi, M. & Hooper, A., 2018. Inversion of Surface Deformation Data for Rapid Estimates of Source Parameters and Uncertainties: A Bayesian Approach, *Geochemistry, Geophysics, Geosystems*, **19**(7), 2194–2211.

Bato, M. G., Pinel, V., & Yan, Y., 2017. Assimilation of Deformation Data for Eruption Forecasting: Potentiality Assessment Based on Synthetic Cases, *Frontiers in Earth Science*, **5**.

Battaglia, M., Cervelli, P. F., & Murray, J. R., 2013. dMODELS: A MATLAB software package for modeling crustal deformation near active faults and volcanic centers, *Journal of Volcanology and Geothermal Research*, **254**, 1–4.

Beauducel, F., Lafon, D., Béguin, X., Saurel, J.-M., Bosson, A., Mallarino, D., Boissier, P., Brunet, C., Lemarchand, A., Anténor-Habazac, C., Nercessian, A., & Fahmi, A. A., 2020a. Webobs: The volcano observatories missing link between research and real-time monitoring, *Frontiers in Earth Science*, **8**.

Beauducel, F., Peltier, A., Villié, A., & Suryanto, W., 2020b. Mechanical imaging of a volcano plumbing system from GNSS unsupervised modeling, *Geophysical Research Letters*, **47**(17), e2020GL089419.

Biggs, J. & Pritchard, M. E., 2017. Global Volcano Monitoring: What Does It Mean When Volcanoes Deform?, *Elements*, **13**(1), 17–22.

Bonafede, M. & Ferrari, C., 2009. Analytical models of deformation and residual gravity changes due to a Mogi source in a viscoelastic medium, *Tectonophysics*, **471**(1-2), 4–13.

Bruno, V., Aloisi, M., Gambino, S., Mattia, M., Ferlito, C., & Rossi, M., 2022. The Most Intense Deflation of the Last Two Decades at Mt. Etna: The 2019-2021 Evolution of Ground Deformation and Modeled Pressure Sources, *Geophysical Research Letters*, **49**(6), e2021GL095195.

Cannavó, F., 2019. A new user-friendly tool for rapid modelling of ground deformation, *Computers & Geosciences*, **128**, 60–69.

Caricchi, L., Townsend, M., Rivalta, E., & Namiki, A., 2021. The build-up and triggers of volcanic eruptions, *Nature Reviews Earth & Environment*, **2**(7), 458–476.

Cervelli, P. F., 2013. Analytical expressions for deformation from an arbitrarily oriented spheroid in a half-space, in *AGU Fall Meeting Abstracts*, vol. 2013, pp. V44C–06.

Cesca, S., Letort, J., Razafindrakoto, H. N., Heimann, S., Rivalta, E., Isken, M. P., Nikkhoo, M., Passarelli, L.,

659   Petersen, G. M., Cotton, F., & Dahm, T., 2020. Drainage of a deep magma reservoir near Mayotte inferred
660   from seismicity and deformation, *Nature Geoscience*, **13**(1), 87–93.

661   Comninou, M. & Dundurs, J., 1975. The angular dislocation in a half space, *Journal of Elasticity*, **5**(3–4),
662   203–216.

663   Crouch, S. L., 1976. Solution of plane elasticity problems by the displacement discontinuity method. I. Infinite
664   body solution, *International Journal for Numerical Methods in Engineering*, **10**(2), 301–343.

665   Crouch, S. L. & Starfield, A. M., 1983. *Boundary Element Method in Solid Mechanics*, Allen and Unwin,
666   London.

667   Davis, P., Hastie, L., & Stacey, F., 1974. Stresses within an active volcano—with particular reference to
668   Kilauea, *Tectonophysics*, **22**(3-4), 355–362.

669   Davis, P. M., 1983. Surface deformation associated with a dipping hydrofracture, *Journal of Geophysical*
670   *Research: Solid Earth*, **88**(B7), 5826–5834.

671   Davis, P. M., 1986. Surface deformation due to inflation of an arbitrarily oriented triaxial ellipsoidal cavity
672   in an elastic half-space, with reference to Kilauea volcano, Hawaii, *Journal of Geophysical Research: Solid*
673   *Earth*, **91**(B7), 7429–7438.

674   Davis, T., Bagnardi, M., Lundgren, P., & Rivalta, E., 2021. Extreme Curvature of Shallow Magma Pathways
675   Controlled by Competing Stresses: Insights From the 2018 Sierra Negra Eruption, *Geophysical Research*
676   *Letters*, **48**(13), e2021GL093038, e2021GL093038 2021GL093038.

677   Degruyter, W., Parmigiani, A., Huber, C., & Bachmann, O., 2019. How do volatiles escape their shallow mag-
678   matic hearth?, *Philosophical Transactions of the Royal Society A: Mathematical, Physical and Engineering*
679   *Sciences*, **377**(2139), 20180017.

680   Dumont, S., Sigmundsson, F., Parks, M. M., Drouin, V. J. P., Pedersen, G. B. M., Jónsdóttir, I., Höskuldsson,
681   Á., Hooper, A., Spaans, K., Bagnardi, M., Gudmundsson, M. T., Barsotti, S., Jónsdóttir, K., Högnadóttir, T.,
682   Magnússon, E., Hjartardóttir, Á. R., Dürig, T., Rossi, C., & Oddsson, B., 2018. Integration of SAR Data Into
683   Monitoring of the 2014-2015 Holuhraun Eruption, Iceland: Contribution of the Icelandic Volcanoes Supersite
684   and the FutureVolc Projects, *Frontiers in Earth Science*, **6**.

685   Dvorak, J. J. & Dzurisin, D., 1997. Volcano geodesy: The search for magma reservoirs and the formation of
686   eruptive vents, *Reviews of Geophysics*, **35**(3), 343–384.

687   Dzurisin, D., 2000. Volcano geodesy: challenges and opportunities for the 21st century, *Philosophical Transac-*
688   *tions of the Royal Society of London. Series A: Mathematical, Physical and Engineering Sciences*, **358**(1770),
689   1547–1566.

690   Dzurisin, D., 2003. A comprehensive approach to monitoring volcano deformation as a window on the eruption
691   cycle, *Reviews of Geophysics*, **41**(1).

692   Dzurisin, D., 2006. *Volcano deformation: new geodetic monitoring techniques*, Springer Science & Business
693   Media.

694   Edmonds, M. & Woods, A. W., 2018. Exsolved volatiles in magma reservoirs, *Journal of Volcanology and*
695   *Geothermal Research*, **368**, 13–30.

Eshelby, J. D., 1957. The determination of the elastic field of an ellipsoidal inclusion, and related problems, *Proceedings of the royal society of London. Series A. Mathematical and physical sciences*, **241**(1226), 376–396.

Fialko, Y., Khazan, Y., & Simons, M., 2001. Deformation due to a pressurized horizontal circular crack in an elastic half-space, with applications to volcano geodesy, *Geophysical Journal International*, **146**(1), 181–190.

Furuya, M., 2004. Localized deformation at miyakejima volcano based on jers-1 radar interferometry: 1992–1998, *Geophysical Research Letters*, **31**(5).

Furuya, M., 2005. Quasi-static thermoelastic deformation in an elastic half-space: theory and application to InSAR observations at Izu-Oshima volcano, Japan, *Geophysical Journal International*, **161**(1), 230–242.

Harris, J. W. & Stöcker, H., 1998. *Handbook of mathematics and computational science*, Springer Science & Business Media.

Heimann, S., Vasyura-Bathke, H., Sudhaus, H., Isken, M. P., Kriegerowski, M., Steinberg, A., & Dahm, T., 2019. A Python framework for efficient use of pre-computed Green's functions in seismological and other physical forward and inverse source problems, *Solid Earth*, **10**(6), 1921–1935.

Hill, D., Montgomery-Brown, E., Shelly, D., Flinders, A., & Prejean, S., 2020. Post-1978 tumescence at Long Valley Caldera, California: A geophysical perspective, *Journal of Volcanology and Geothermal Research*, **400**, 106900.

Kern, W. F. & Bland, J. R., 1938. *Solid mensuration: with proofs*, J. Wiley & Sons, Incorporated.

Klein, P. P., 2012. On the ellipsoid and plane intersection equation, *Applied Mathematics*, **3**(11), 1634–1640.

Kobayashi, T., Morishita, Y., & Munekane, H., 2018. First detection of precursory ground inflation of a small phreatic eruption by InSAR, *Earth and Planetary Science Letters*, **491**, 244–254.

Kuriyama, K. & Mizuta, Y., 1993. Three-dimensional elastic analysis by the displacement discontinuity method with boundary division into triangular leaf elements, *International Journal of Rock Mechanics and Mining Sciences & Geomechanics Abstracts*, **30**(2), 111–123.

Langbein, J., Dzurisin, D., Marshall, G., Stein, R., & Rundle, J., 1995. Shallow and peripheral volcanic sources of inflation revealed by modeling two-color geodimeter and leveling data from Long Valley Caldera, California, 1988–1992, *Journal of Geophysical Research: Solid Earth*, **100**(B7), 12487–12495.

Lipschutz, M. M., 1969. *Schaum's outline of theory and problems of differential geometry*, McGraw-Hill, New York.

Lisowski, M., 2007. *Analytical volcano deformation source models*, pp. 279–304, Springer Berlin Heidelberg, Berlin, Heidelberg.

Lisowski, M., Dzurisin, D., Denlinger, R. P., & Iwatsubo, E. Y., 2008. Analysis of GPS-measured deformation associated with the 2004–2006 dome-building eruption of Mount St. Helens, Washington, in *A Volcano Rekindled: The Renewed Eruption of Mount St. Helens, 2004–2006*, vol. 1750, pp. 301–333, US Geological Survey Reston, Virginia.

Lisowski, M., McCaffrey, R., Wicks, C. W., & Dzurisin, D., 2021. Geodetic Constraints on a 25-year Mag-

matic Inflation Episode Near Three Sisters, Central Oregon, *Journal of Geophysical Research: Solid Earth*, **126**(12), e2021JB022360, e2021JB022360 2021JB022360.

Lu, Z. & Dzurisin, D., 2014. *Role of Ground Surface Deformation in Volcano Monitoring*, pp. 71–85, Springer Berlin Heidelberg, Berlin, Heidelberg.

Mastin, L. G., Roeloffs, E., Beeler, N. M., & Quick, J. E., 2008. Constraints on the size, overpressure, and volatile content of the Mount St. Helens magma system from geodetic and dome-growth measurements during the 2004-2006+ eruption, Tech. rep., US Geological Survey.

McTigue, D., 1987. Elastic stress and deformation near a finite spherical magma body: resolution of the point source paradox, *Journal of Geophysical Research: Solid Earth*, **92**(B12), 12931–12940.

Mindlin, R. D., 1936. Force at a point in the interior of a semi-infinite solid, *physics*, **7**(5), 195–202.

Mogi, K., 1958. Relations between the eruptions of various volcanoes and the deformations of the ground surfaces around them, *Earthq Res Inst*, **36**, 99–134.

Narita, S., Murakami, M., & Tanaka, R., 2019. Quantitative relationship between plume emission and multiple deflations after the 2014 phreatic eruption at Ontake volcano, Japan, *Earth, Planets and Space*, **71**(145), 1–16.

Narita, S., Ozawa, T., Aoki, Y., Shimada, M., Furuya, M., Takada, Y., & Murakami, M., 2020. Precursory ground deformation of the 2018 phreatic eruption on Iwo-Yama volcano, revealed by four-dimensional joint analysis of airborne and spaceborne InSAR, *Earth, Planets and Space*, **72**(145), 1–16.

Nikkhoo, M. & Rivalta, E., 2022. Analytical Solutions for Gravity Changes Caused by Triaxial Volumetric Sources, *Geophysical Research Letters*, **49**(8), e2021GL095442, e2021GL095442 2021GL095442.

Nikkhoo, M. & Walter, T. R., 2015. Triangular dislocation: an analytical, artefact-free solution, *Geophysical Journal International*, **201**(2), 1119–1141.

Nikkhoo, M., Walter, T. R., Lundgren, P. R., & Prats-Iraola, P., 2017. Compound dislocation models (CDMs) for volcano deformation analyses, *Geophysical Journal International*, **208**(2), 877–894.

Okada, Y., 1985. Surface deformation due to shear and tensile faults in a half-space, *Bulletin of the seismological society of America*, **75**(4), 1135–1154.

Okubo, S., 1991. Potential and gravity changes raised by point dislocations, *Geophysical journal international*, **105**(3), 573–586.

Peltier, A., Ferrazzini, V., Di Muro, A., Kowalski, P., Villeneuve, N., Richter, N., Chevrel, O., Froger, J. L., Hrysiewicz, A., Gouhier, M., Coppola, D., Retailleau, L., Beauducel, F., Gurioli, L., Boissier, P., Brunet, C., Catherine, P., Fontaine, F., Lauret, F., Garavaglia, L., Lebreton, J., Canjamale, K., Desfete, N., Griot, C., Harris, A., Arellano, S., Liuzzo, M., Gurrieri, S., & Ramsey, M., 2020. Volcano Crisis Management at Piton de la Fournaise (La Réunion) during the COVID-19 Lockdown, *Seismological Research Letters*, **92**(1), 38–52.

Pinel, V., Poland, M., & Hooper, A., 2014. Volcanology: Lessons learned from Synthetic Aperture Radar imagery, *Journal of Volcanology and Geothermal Research*, **289**, 81–113.

Poland, M. P. & Zebker, H. A., 2022. Volcano geodesy using InSAR in 2020: the past and next decades, *Bulletin of Volcanology*, **84**(27).

Rivalta, E. & Segall, P., 2008. Magma compressibility and the missing source for some dike intrusions, *Geophysical Research Letters*, **35**(4).

Salzer, J. T., Nikkhoo, M., Walter, T. R., Sudhaus, H., Reyes-Dávila, G., Bretón, M., & Arámbula, R., 2014. Satellite radar data reveal short-term pre-explosive displacements and a complex conduit system at volcÃ¡n de colima, mexico, *Frontiers in Earth Science*, **2**.

Segall, P., 2010. *Earthquake and volcano deformation*, Princeton University Press.

Segall, P., 2016. Repressurization following eruption from a magma chamber with a viscoelastic aureole, *Journal of Geophysical Research: Solid Earth*, **121**(12), 8501–8522.

Segall, P., Cervelli, P., Owen, S., Lisowski, M., & Miklius, A., 2001. Constraints on dike propagation from continuous GPS measurements, *Journal of Geophysical Research: Solid Earth*, **106**(B9), 19301–19317.

Sigmundsson, F., Hooper, A., Hreinsdóttir, S., Vogfjörd, K. S., Ófeigsson, B. G., Heimisson, E. R., Dumont, S., Parks, M., Spaans, K., Gudmundsson, G. B., et al., 2015. Segmented lateral dyke growth in a rifting event at Bárðarbunga volcanic system, Iceland, *Nature*, **517**(7533), 191–195.

Sun, R. J., 1969. Theoretical size of hydraulically induced horizontal fractures and corresponding surface uplift in an idealized medium, *Journal of Geophysical Research (1896-1977)*, **74**(25), 5995–6011.

Trasatti, E., 2022. Volcanic and seismic source modeling: An open tool for geodetic data modeling, *Frontiers in Earth Science*, **10**.

Trasatti, E., Acocella, V., Di Vito, M. A., Del Gaudio, C., Weber, G., Aquino, I., Caliro, S., Chiodini, G., de Vita, S., Ricco, C., & Caricchi, L., 2019. Magma Degassing as a Source of Long-Term Seismicity at Volcanoes: The Ischia Island (Italy) Case, *Geophysical Research Letters*, **46**(24), 14421–14429.

Ueda, H., Nagai, M., & Tanada, T., 2018. Phreatic eruptions and deformation of Ioto Island (Iwo-jima), Japan, triggered by deep magma injection, *Earth, Planets and Space*, **70**(38), 1–15.

Vasyura-Bathke, H., Dettmer, J., Steinberg, A., Heimann, S., Isken, M. P., Zielke, O., Mai, P. M., Sudhaus, H., & Jónsson, S., 2019. Beat: Bayesian earthquake analysis tool, Tech. rep.

Vasyura-Bathke, H., Dettmer, J., Steinberg, A., Heimann, S., Isken, M. P., Zielke, O., Mai, P. M., Sudhaus, H., & Jónsson, S., 2020. The Bayesian earthquake analysis tool, *Seismological Research Letters*, **91**(2A), 1003–1018.

Wang, R., Lorenzo-Martin, F., & Roth, F., 2006. PSGRN/PSCMP—a new code for calculating co-and post-seismic deformation, geoid and gravity changes based on the viscoelastic-gravitational dislocation theory, *Computers & Geosciences*, **32**(4), 527–541.

Wang, T., Shi, Q., Nikkhoo, M., Wei, S., Barbot, S., Dreger, D., Bürgmann, R., Motagh, M., & Chen, Q.-F., 2018. The rise, collapse, and compaction of Mt. Mantap from the 3 September 2017 North Korean nuclear test, *Science*, **361**(6398), 166–170.

Wang, X. & Aoki, Y., 2019. Posteruptive thermoelastic deflation of intruded magma in usu volcano, japan, 1992–2017, *Journal of Geophysical Research: Solid Earth*, **124**(1), 335–357.

Wasser, V. K., Lopez, T. M., Anderson, K. R., Izbekov, P. E., & Freymueller, J. T., 2021. Multidisciplinary Constraints on Magma Compressibility, the Pre-Eruptive Exsolved Volatile Fraction, and the H_2O/CO_2

Molar Ratio for the 2006 Augustine Eruption, Alaska, *Geochemistry, Geophysics, Geosystems*, **22**(9), e2021GC009911.

Wicks, C. W., Dzurisin, D., Lowenstern, J. B., & Svarc, J., 2020. Magma Intrusion and Volatile Ascent Beneath Norris Geyser Basin, Yellowstone National Park, *Journal of Geophysical Research: Solid Earth*, **125**(2), e2019JB018208, e2019JB018208 2019JB018208.

Xu, W., Jónsson, S., Corbi, F., & Rivalta, E., 2016. Graben formation and dike arrest during the 2009 Harrat Lunayyir dike intrusion in Saudi Arabia: Insights from InSAR, stress calculations and analog experiments, *Journal of Geophysical Research: Solid Earth*, **121**(4), 2837–2851.

Xu, W., Xie, L., Aoki, Y., Rivalta, E., & Jónsson, S., 2020. Volcano-wide deformation after the 2017 erta ale dike intrusion, ethiopia, observed with radar interferometry, *Journal of Geophysical Research: Solid Earth*, **125**(8), e2020JB019562.

Yang, X.-M., Davis, P. M., & Dieterich, J. H., 1988. Deformation from inflation of a dipping finite prolate spheroid in an elastic half-space as a model for volcanic stressing, *Journal of Geophysical Research: Solid Earth*, **93**(B5), 4249–4257.

Yoffe, E. H., 1960. The angular dislocation, *Philosophical Magazine*, **5**(50), 161–175.

Yunjun, Z., Amelung, F., & Aoki, Y., 2021. Imaging the Hydrothermal System of Kirishima Volcanic Complex With L-Band InSAR Time Series, *Geophysical Research Letters*, **48**(11), e2021GL092879, e2021GL092879 2021GL092879.

Zhan, Y., Gregg, P. M., Chaussard, E., & Aoki, Y., 2017. Sequential Assimilation of Volcanic Monitoring Data to Quantify Eruption Potential: Application to Kerinci Volcano, Sumatra, *Frontiers in Earth Science*, **5**.

This paper has been produced using the Blackwell Scientific Publications GJI LATEX2e class file.